Chem. Rev. **2003,** *103,* 4963−4984

Atmospheric Chemistry of Meteoric Metals

John M. C. Plane

School of Environmental Sciences, University of East Anglia, Norwich NR4 7TJ, United Kingdom

Received April 14, 2003

Contents

1. Introduction

The subject of this review is the atmospheric chemistry of the metals that ablate from meteoroids at altitudes between 70 and 120 km in the Earth's atmosphere. Before describing the many unusual phenomena that arise from this extraterrestrial input of material, the review will begin with a general introduction to the chemistry and physics of this region of the atmosphere. This introduction will be reasonably detailed because many readers, indeed even a significant fraction of atmospheric chemists, have little knowledge of the atmospheric regions above the stratosphere. Figure 1a is a temperature profile of the atmosphere from 0 to 120 km, which historically has been used to define the regions of the atmosphere. The region extending from about 75 to 110 km is often referred to as the mesosphere/lower thermosphere (MLT) region. The MLT is of particular interest because it forms the boundary between the atmosphere and space and is subject to high-energy inputs from above in the form of solar electromagnetic radiation and the solar wind, and a nearly equivalent amount of energy from below in the form of gravity waves, tides and planetary waves.

John Plane was born in 1958 and raised in South Africa. He obtained his M.A. degree in Natural Sciences, followed by his Ph.D. degree in Physical Chemistry, at Cambridge University between 1976 and 1983. He was a Research Fellow at St. John's College, Cambridge, from 1982 to 1985 and then went to the Rosenstiel School of Marine and Atmospheric Science, University of Miami, where he was Assistant and then Associate Professor. In 1991 he moved to the School of Environmental Sciences, University of East Anglia, becoming a Reader in 1994 and Professor of Environmental Science in 1999.

The mesosphere begins at the stratopause around 50 km, a region characterized by a local temperature maximum caused by heating due to stratospheric ozone absorbing solar UV radiation above 200 nm. Figure 1b is a height-versus-latitude plot of temperature during mid-summer in the northern hemisphere. This shows that the temperature decreases with height through the mesosphere up to the mesopause (85−100 km depending on season), which is actually the coldest region of the planet. Above the mesopause the thermosphere begins. The absorption of extreme UV and X-ray radiation at wavelengths below 180 nm, mostly by O_2, leads to a rapid warming with altitude. Temperatures in the thermosphere reach 400−1000 K, although it should be noted that these are kinetic temperatures; the vibrational (and sometimes rotational) modes of molecules are not usually in local thermodynamic equilibrium (LTE) because of the low pressure ($<10^{-7}$ bar) above 110 km.

The low temperatures in the mesosphere are caused by limited local heating, since most solar EUV is removed in the thermosphere, and the pressure range in the mesosphere (10^{-6}−10^{-3} bar) is too low for O_3 to form efficiently through the recombination

10.1021/cr0205309 CCC: $44.00

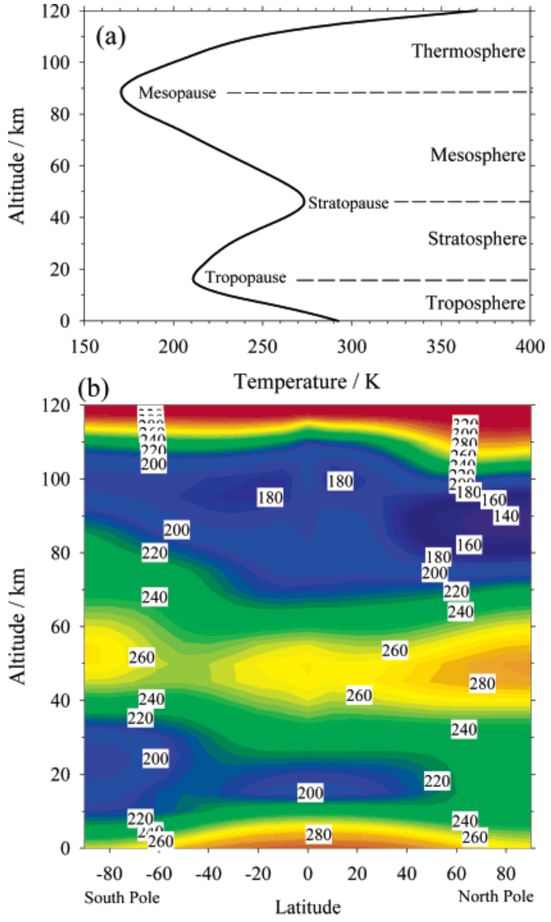

Figure 1. (a) Temperature profile between 0 and 120 km for July, 40°N, identifying the regions of the atmosphere. (b) Plot of temperature (K) as a function of altitude and latitude during July. Source: MSIS-E−90 model (http://nssdc.gsfc.nasa.gov/space/model/models/msis).

of O and O_2, in contrast with the stratosphere. A further consequence of the low pressures is that greenhouse gases, principally CO_2, act as infrared radiators that contribute directly to the cooling of the MLT region. Figure 1b also shows that unlike the lower atmosphere, which is warmer in summer, the coldest part of the MLT region is actually the *summer* mesopause around 85 km. The explanation for this surprising observation appears to be the effect of gravity waves, which originate in the troposphere from a variety of sources, including orographic forcing, cumulo-nimbus storms, and cyclonic fronts. Much of the energy and momentum flux of these waves is filtered out in the stratosphere, but a significant portion of the shorter period waves propagate to the upper mesosphere. As a wave travels upward through the mesosphere, the wave amplitude increases with falling pressure until the wave becomes unstable and breaks, depositing both energy and momentum in the MLT. This exerts a drag on the zonal wind, resulting in a southward meridional flow (during summer in the northern hemisphere), as shown in Figure 2. The upwelling air at northern high latitudes which feeds this meridional flow is cooled by adiabatic expansion, leading to very low temperatures which can fall below 120 K. Indeed, if the summer mesopause at high latitudes were in thermal equilibrium, it would have a temperature around 220 K. A striking feature of this meridional circulation is that air from the entire global mesosphere is then funneled down into the lower stratosphere within the Antarctic polar vortex (Figure 2). The consequences of this will be considered in section 6.5. As shown in Figure 1b, the winter mesopause occurs around 100 km, about 15 km higher than in summer.

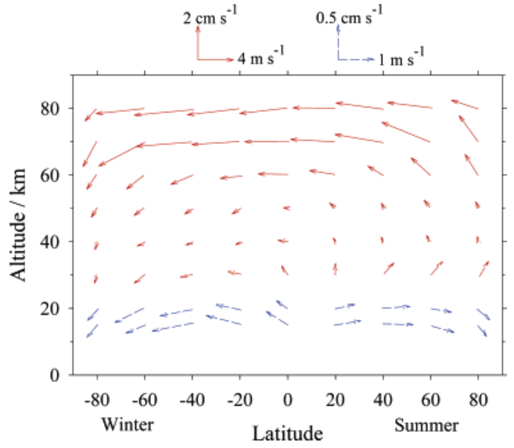

Figure 2. Meridional wind vectors as a function of altitude and latitude during July. (Adapted from Shimazaki T. *Minor Constituents in the Middle Atmosphere;* D. Reidel, Dordrecht, 1985.).

There are several important consequences of the very low pressures in the MLT region. First, the mean free path of the air molecules approaches 1 m at a height of 110 km. Bulk motion of the air cannot then be sustained, and molecular diffusion dominates. The transition region around 105 km is known as the turbopause and is a useful working definition of the boundary between the atmosphere and space. In the absence of bulk motion above the turbopause, separation of molecules by mass is able to occur through gravitational settling of the heavier species, so that only H, H_2, and He occur at significant concentrations above 500 km.

A second consequence of very low pressures is on the chemistry of the MLT region. Atomic oxygen is the major reactive species in this region, the rate-determining step in its removal being the recombination reaction between O and O_2 to form O_3. The rate of this reaction, at its low-pressure limit, is pressure dependent: above 82 km the time constant for O removal exceeds 12 h, so that an active radical chemistry persists throughout the night. Figure 3 illustrates vertical profiles of the mixing ratios (i.e., mole fractions) of a selection of major and minor constituents in the MLT region. An important reason for plotting the mixing ratio rather than the concentration is that in the region of bulk mixing below the turbopause, the mixing ratio of a chemically inert species (e.g., Ar or CO_2) remains constant with height, whereas an increase or decrease in the mixing ratio of a species indicates a local source or sink, respectively.

Figure 3b shows that atomic O is the dominant reactive species. It is produced during the day by the photolysis of O_2, mostly by absorption in the Schumann−Runge continuum (130−175 nm) and the Schumann−Runge bands (175−195 nm). Atomic O

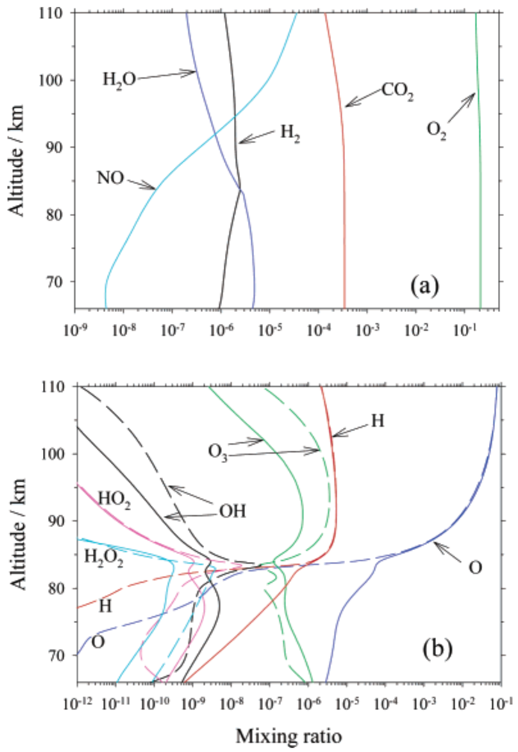

Figure 3. Vertical profiles of the mixing ratios of atmospheric constituents in the mesosphere and lower thermosphere: (a) species with no diurnal variation; (b) reactive species with significant diurnal variations, where broken lines indicate the nighttime profiles. Profiles calculated using the UEA 1-dimensional mesospheric model for 40°N in January.

is removed principally by the sequence of reactions 1−5

$$O + O_2\ (+M) \rightarrow O_3,\ \text{where } M = \text{third body}\ (N_2 \text{ and } O_2) \quad (1)$$

$$H + O_3 \rightarrow OH + O_2 \quad (2)$$

$$O + OH \rightarrow H + O_2 \quad (3)$$

$$H + O_2\ (+M) \rightarrow HO_2 + M \quad (4)$$

$$O + HO_2 \rightarrow OH + O_2 \quad (5)$$

$$H + HO_2 \rightarrow H_2 + O_2 \quad (6)$$

Note that whereas there is a very large difference between the daytime and nighttime levels of O below 82 km, above this height there is little diurnal variation: the chemical energy built up by solar UV absorption during the day is stored and available for slow release throughout the night. The sharp transition in the profile between 75 and 85 km is known as the atomic oxygen shelf.

Atomic H is produced from the photolysis of H_2O, which is mainly formed in the lower mesosphere from the oxidation of CH_4 propagating up from the stratosphere. H has a similar profile to O, with a pronounced diurnal variation below 82 km (Figure 3b). Eventually, H_2 is formed through reaction 6, leading to an increase in the H_2 mixing ratio up to about 90 km. Inspection of Figure 3a shows that the H_2O mixing ratio decreases markedly throughout the MLT above 80 km. This is due to photolysis by solar Lyman-α radiation at 121.6 nm, which is able to penetrate down to about 80 km because the absorption cross-section of O_2 happens to be very small right at the Lyman-α wavelength. The O_3 minimum above 80 km is caused by two catalytic cycles involving H (reactions 2 + 3, and reactions 4 + 5 + 3). Note that O_3 has a pronounced diurnal variation above 80 km with a nighttime maximum (Figure 3b).

Figure 3a reveals that nitric oxide (NO) has a significant source in the lower thermosphere. This arises mainly from the reaction of electronically excited nitrogen atoms

$$N(^2D) + O_2 \rightarrow NO + O \quad (7)$$

where $N(^2D)$ is produced from a variety of exothermic ion−molecule reactions (e.g., $N_2^+ + O \rightarrow N(^2D) + NO^+$). Production of NO via reaction 7 results in a substantial flux into the mesosphere and stratosphere.

Another important aspect of the MLT is that this region is exposed to solar photons that are energetic enough to ionize molecules and atoms, forming significant plasma concentrations above 70 km, which is where the ionosphere begins. The electron density profile is divided up into three regions, based on historical observations using ground-based ionosondes. In the *D* region (70−95 km), proton hydrates (i.e., $H^+(H_2O)_n$, $n \geq 1$) and negative ions dominate. Higher up in the *E* region (95−170 km), O_2^+ and NO^+ are the dominant ions, balanced by free electrons. Above this in the *F* region (170−500 km), O^+ and N^+ ions dominate.

Figure 4 illustrates the profiles of electrons and the major positive ions up to 140 km and also shows that the electron density exhibits a pronounced diurnal variation. This is because the primary source of ions and electrons in the lower *E* region above 100 km is solar X-ray and extreme ultraviolet radiation (EUV) at $\lambda < 103$ nm. Important components of this are the Lyman-β (102.6 nm) line, the C III line (97.7 nm), the He I and II lines at 58.4 and 30.4 nm, and soft X-rays at $\lambda < 1$ nm. The photoionization of NO by Lyman-α is the main source of plasma below 90 km. Galactic cosmic rays are a significant source of ionization in the lower mesosphere.

In the *E* region, O_2^+ and N_2^+ are the major primary ions formed by photoionization. However, N_2^+ is rapidly lost by reacting with either O or O_2 to form NO^+ or O_2^+, respectively. In the *D* region, the higher atmospheric density allows recombination reactions to become significant. In the case of positive ions, this causes clustering, initially by N_2, O_2, and CO_2, but these weak ligands eventually switch with H_2O to form hydrates. Electrons are also able to attach to O_2 and react with O_3 to form the negative ions O_2^- and O^-, respectively, which eventually form more stable negative ions such as HCO_3^-, NO_3^-, and Cl^- (from stratospheric HCl). The ion chemistry of the *D* region is therefore extremely complex in comparison with the *E* or *F* regions. Note that above 85 km, negative ions are destroyed rapidly either by photo-

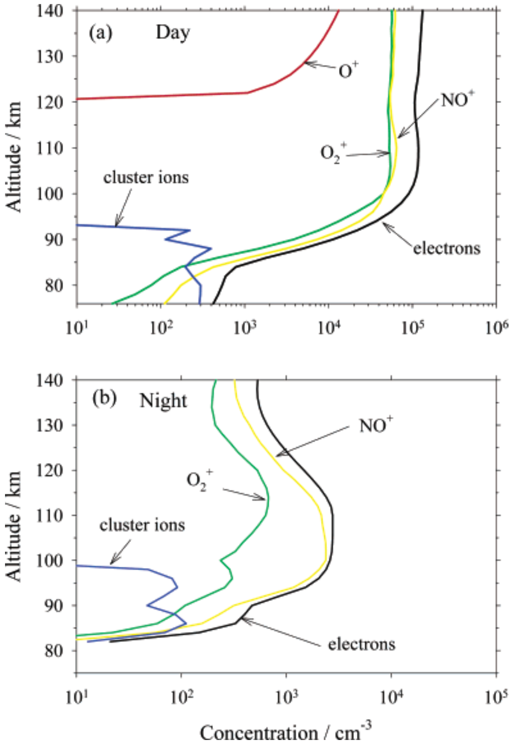

Figure 4. Vertical profiles of the electron and major positive ion densities in the mesosphere and lower thermosphere during January 1999: (a) daytime, (b) nighttime. Source: IRI-95 Reference model (http://nssdc.gsfc.nasa.gov/space/model/models/iri).

detachment or by associative attachment (e.g., $O_2^- + O \rightarrow O_3 + e^-$) in the presence of large concentrations of O.

It has been known for more than 50 years that neutral metal atoms such as Na are present in the upper atmosphere. Radiation in the nightglow spectrum at 589 nm was first reported by Slipher in 1929,[1] and 10 years later it was established that this radiation was due to the transition $Na(3^2P_J - 3^2S_{1/2})$ and that the source was located within the Earth's atmosphere.[2] Over the next 60 years, these observations have raised a number of important questions. For instance, is the major source of the metals extraterrestrial or from the Earth's surface? Why do the metals appear as layers of neutral metal atoms at about 90 km, and why are these layers only a few kilometers thick? Why is the relative abundance of the metals in the layers quite different from their relative abundances in common types of meteorites? How can the different seasonal behavior of the metals be explained? What is the source of metal atoms from which sudden or sporadic layers form, often explosively? How do dynamical processes, such as atmospheric gravity waves and tides, affect the chemistry that governs the metal layers? Finally, do the metal layers act as sensitive indicators of climate change in the mesosphere, either directly or through their relationship with noctilucent clouds, and do the metals have any impact in the stratosphere and troposphere?

To answer these questions, a comprehensive understanding of the chemistry which these metals undergo in the upper atmosphere is required. Substantial progress has in fact been made in this area during the last 20 years, through a combination of laboratory studies and atmospheric modeling. It should be noted that a general review of meteoric metals in the upper atmosphere was published by the author in 1991;[3] this was followed by reviews of laboratory studies on metal reactions in 1994[4] and 2002[5] and a review of atmospheric modeling of metals in 2002.[6]

The present review is divided into five sections following the Introduction. Section 2 discusses the process of meteoric ablation as the source of metals in the MLT. Section 3 describes the techniques used to observe the metal atom layers in the upper mesosphere and identifies many of their remarkable features. Section 4 describes the specialized laboratory techniques and theoretical formalisms that have been developed to study the reaction kinetics and photochemistry of metallic species under mesospheric conditions. Section 5 discusses atmospheric modeling of metals in the MLT, including a treatment of gravity wave interactions with the metal layers. Section 6 describes a number of atmospheric phenomena involving metals: the Na *D*-line airglow, persistent meteor trains, sporadic layers, climate change indicators with an emphasis on noctilucent clouds, and the effects of meteoric smoke in the middle and lower atmosphere.

2. Meteoric Ablation as the Source of Mesospheric Metals

There are two principal sources of meteoroids in the Earth's atmosphere.[7,8] First are the dust trails produced by sublimating comets as they orbit the sun. These trails are the origin of meteor showers such as the Perseids and Leonids.[9] Second are fragments from the asteroid belt beyond Mars and dust particles from long-decayed cometary trails. These give rise to the continuous input of sporadic meteoroids that provides a much greater mass flux than the showers.[7,8] Unfortunately, the average daily input of meteoroids into the atmosphere is a rather uncertain quantity. Until the 1990s, estimates of the mass flux passing through the beams of meteor radars indicated a figure of about 44 t d^{-1} over the entire Earth.[10] However, a conventional meteor radar measures specular reflections from the ion trail created in the atmosphere by the ablating meteoroid—the mass and velocity of the meteoroid are derived somewhat indirectly from this signal.[11] Furthermore, the wavelength of the radar will only sample a subset of the mass/velocity distribution of the meteoroids. In fact, the mass flux from conventional radar estimates has now been revised upward by a factor of 2−3.[12]

The mass flux has also been estimated in other ways. For instance, measuring the accumulation of iridium in ocean-floor sediments indicates that the meteoric influx could be up to 240 t d^{-1}.[13] More recently, the analysis of small particle impact craters on the Long Duration Exposure Facility (LDEF), an orbital impact detector placed on a spacecraft for several years, has yielded an estimate of 130 t d^{-1}.[14,15] The median mass of the incoming dust particles was deduced to be 10 μg, with a median radius of 100 μm and a mean entry velocity of about 18 km s^{-1}. Single-particle analyses of stratospheric aerosol have shown that one-half of the particles in the lower stratosphere contain 0.5−1.0 wt % meteoric iron by mass, requiring a total extraterrestrial flux of between 20 and 100 t d^{-1}.[16]

In the past couple of years, high-powered large aperture radars, such as the radio telescope at Arecibo, have reported direct observations of the meteor head echo (i.e., the ball of plasma around the ablating particle as it descends through the atmosphere). This enables measurements of the direction of origin, velocity, deceleration, and mass to be made.[17−21] The observed mass distribution is shifted to smaller mass ranges (median mass 1 μg) compared to the LDEF results, so that the total incoming mass is about 1 order of magnitude lower than the LDEF estimate.[15] The mean entry velocity also seems to be significantly higher, around 40−50 km s^{-1}. These conflicting results from the two different types of radar measurement have yet to be resolved. It should be noted that particles which originate within the solar system must have entry velocities that range from 11.5 km s^{-1} for a particle in the same orbit as the Earth to 72 km s^{-1} for a particle in a retrograde orbit.[7]

Because of their very high entry velocities, meteoroids undergo rapid frictional heating by collision with air molecules, and their constituent minerals subsequently vaporize. The physics of this process has been treated in detail by several investigators.[22−24] The problem becomes manageable for particles less than about 250 μm in radius, because heat conductivity through the particle is fast enough for the particle to be treated as isothermal.[22] Most of the total mass of cosmic dust is made up from particles with masses less than 100 μg.[15] Assuming a density of 2 g cm^{-3} (typical of an ordinary chondrite), a 250 μm meteoroid has a mass of 130 μg, thereby justifying the neglect of heat conductivity.

The frictional heating of the meteoroid by collisions with air molecules is balanced by radiative losses and by the absorption of heat energy through temperature increases, melting, phase transitions, and vaporization. To calculate these terms, parameters such as the meteoroid shape, density, and composition are needed. The question of composition has been discussed in detail recently.[25,26] There is some uncertainty here because of the great variability in composition of the different types of meteorites.[25] Furthermore, it may be that the composition of the meteoroids that ablate in the upper atmosphere is different from that of the meteorites that survive transit through the atmosphere.[25] Nevertheless, the current working assumption is that most of the extraterrestrial material has the composition of ordinary chondrites.

If the particle is spherical, then the energy balance equation is given by[27]

$$\frac{1}{2}\Lambda\rho_a v^3 = 4\sigma\epsilon(T_s{}^4 - T_a{}^4) + \frac{4}{3}R\rho_m C\,\frac{\partial T_{\mathrm{m}}}{\partial t} \qquad \text{(I)}$$

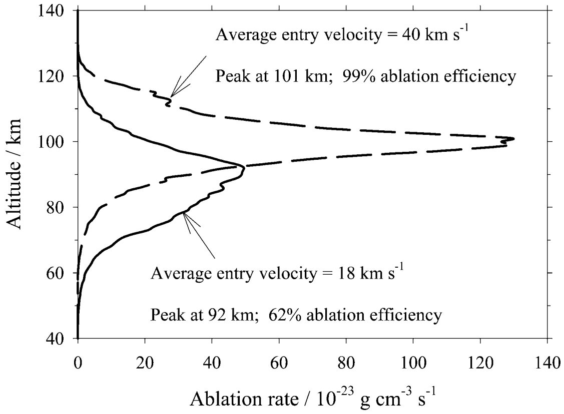

Figure 5. Profiles of the total meteoric ablation rate calculated using the ablation equations in section 2. The solid profile is for the meteoroid mass and velocity distribution derived from the Long Duration Exposure Facility (McBride, N., et al. *Adv. Space Res.* **1999**, *23*, 73). The broken line shows the ablation profile when the entry velocity distribution is shifted upward by 22 km s^{-1}.

The left-hand side of eq I represents the frictional heating term, where Λ is the heat transfer coefficient or fraction of the total kinetic energy of the air molecules that is transferred to the meteoroid, ρ_a is the atmospheric density, and v is the meteoroid velocity. The first term on the right-hand side describes the radiative losses, where is σ Stefan's constant, ϵ is the emissivity of the meteoroid, T_s is the surface temperature of the meteoroid, and T_a is the ambient atmosphere temperature. The second term represents the energy losses due to heat capacity (i.e., vaporization, phase transitions, and heating); R is the meteoroid radius, ρ_m the meteoroid density, C the meteoroid specific heat, T_m the mean temperature of the particle, and t the time. The deceleration of the meteoroid is given by

$$\frac{\mathrm{d}v}{\mathrm{d}t} = \frac{\Gamma\rho_a\pi R^2 v^2}{m} \qquad \text{(II)}$$

where Γ is the atmospheric drag parameter and m is the meteoroid mass.

Inspection of eq I shows that for very small particles, the heat capacity term will be much smaller than the radiative loss term, in which case the meteoroid will not become hot enough to ablate. This is the case for all particles smaller than 100 nm. A 1 μm particle must enter the atmosphere at over 40 km s^{-1} in order to heat up to 1000 K, the temperature at which volatile elements such as Na begin to evaporate.[28] All meteoroids larger than 10 μm will reach this ablation temperature.

In simple ablation models,[6,24] the meteoroid is considered to boil when a temperature around 2000 K is reached. This means that further frictional heat input to the particle is balanced by vaporization and radiative cooling, and no further temperature rise occurs. Figure 5 shows the mass ablation rate as a function of altitude, for the meteoroid mass and velocity distribution from the LDEF experiment.[14] The peak rate of ablation occurs close to 90 km, and about 62% of the total incoming material vaporizes. The unablated fraction consists of particles that are too small, or that enter the atmosphere too slowly, to vaporize completely. Also shown in Figure 5 is the ablation profile predicted if the velocity distribution is shifted to higher velocity so that the mean velocity increases from 18 to 40 km s^{-1}, in line with the large aperture radar measurements[17−20] described above. The ablation profile now peaks just above 100 km, and nearly 100% of the material ablates.

As a starting point, most of the models developed for estimating the meteoric metal input into the atmosphere[3,29] assume that the relative metallic abundances in the ablated vapor are given by their meteoritic abundances. The major metallic constituents by weight are then Mg 12.5%, Fe 11.5%, Al 1.7%, Ni 1.5%, Ca 1.0%, Na 0.6%.[30] A more realistic approach involving fractionation has been proposed recently, with the relatively volatile elements such as Na and K evaporating first around 1000 K and refractory elements (such as Ca) evaporating last.[31] This differential ablation model, which is based on fractionation models used by planetary scientists,[28] was able to explain the large depletion of Ca to Na observed in meteor trails.[32] However, it should be borne in mind that planetary fractionation models are based on equilibrium thermodynamics, whereas the average time during which a meteoroid ablates is about 100 ms, and so kinetic effects such as diffusion may also play a role in governing the efficiency with which particular elements vaporize.

Finally, it should be noted that historically another source of metals in the MLT was postulated to be a layer of dust at about 90 km from which metal atoms are released during the day by thermal evaporation and photosputtering.[3] The proposed origins of this dust have included sea-salt aerosols, volcanic debris, and particles formed from the condensation of refractory species that had evaporated during meteoric ablation.[3] However, there is now strong evidence that direct ablation is the major source of the metal atoms and ions. This evidence includes the good correlation between the relative abundances of metallic ions observed in the lower thermosphere after meteor showers and their elemental abundances in chondritic meteorites,[33,34] sporadic enhancements in the total column abundances of metals during meteor showers,[35] and the direct observation by lidar (section 3.1) of metal atoms in short-lived meteor trails.[32,36−39]

3. Observations of Metals in the MLT Region

3.1. Observational Techniques

The first quantitative observations of metal atoms in the MLT were made in the 1950s using ground-based photometers that measured the resonance fluorescence from spectroscopic transitions of the metal atoms excited by solar radiation.[40] Emission lines from Na, K, Fe, and Ca^+ were successfully observed because these metals have extremely large resonant scattering cross-sections, which is necessary because their concentrations relative to the general atmosphere are less than 100 ppt. Photometry was superseded in the 1970s when the discovery of tuneable laser sources allowed the development of the resonance lidar technique.[3] A pulsed laser beam is tuned to a strongly allowed spectroscopic transition of the metal atom of interest and transmitted up through the atmosphere. The laser pulse is Mie- and Rayleigh-scattered, particularly in the lower atmosphere where there are aerosol layers and the atmospheric density is greater. In the mesosphere the pulse is then resonantly scattered by the metal atoms. A small fraction of the scattered light returns to the ground, where it is collected by a telescope and measured by time-resolved photon counting. The return signal is electronically binned to provide the range, and hence the height, of the scattering layer. The absolute metal density is calibrated from the Rayleigh-scattered signal at a lower altitude of known atmospheric temperature and density.

Lidar has so far been used to observe Na, K, Li, Ca, Ca^+, and Fe.[3] Observations can even be made continuously over a complete diurnal cycle, provided an astronomical quality telescope and narrow band optical filter are employed for daytime measurements.[41] Observations can also be made with extremely good time and height resolution (typically 60 s and 40 m, respectively, for the Na layer), so that the metal layers can be used as tracers of atmospheric motions such as tides and gravity waves.[42,43] In the case of Na and K, a narrow line-width laser can be used in the lidar transmitter to measure temperature and wind profiles in the upper mesosphere.[41,44] This is possible because the absorption spectrum of each D line contains hyperfine structure. For example, the D_2 absorption spectrum of Na consists of six hyperfine resonance lines, which become blended at temperatures above 6 K. The degree of blending is very sensitive to temperature, and so by employing a laser with a tuning accuracy and frequency stability of at least 50 MHz to scan across the D_2 absorption spectrum, the temperature can be measured with an error of $\approx$1 K.[45,46] The laser can also be scanned to the wings of the D_2 absorption peak in order to measure the Doppler shift of the peak. From this the radial wind (i.e., the wind along the line-of-sight of the lidar) can be calculated with an error of less than 3 m s^{-1} and then be resolved into the vertical and horizontal wind components. Recently, a two-color lidar has been used to measure simultaneously the relative populations of the $^5D_4$ and $^5D_3$ spin−orbit multiplets of ground-state Fe, from which the temperature can be derived through the Boltzmann equilibrium.[47]

Resonance lidar has thus become an extremely important tool for studying the chemistry and physics of the MLT. A major reason for this is that the MLT is largely inaccessible to direct measurement. High-altitude aircraft and research balloons reach altitudes of about 22 and 45 km, respectively, whereas satellites cannot operate below 150 km without atmospheric drag causing rapid deceleration and reentry. The only way to sample the MLT in situ is via rocket-borne payloads. However, because the payload traverses the MLT region at a velocity in excess of 1 km s^{-1}, a rocket measurement provides only a very brief snapshot and the instruments must have a rapid time response.[48] Furthermore, contamination from payload outgassing can be a problem, there are restricted sites where rockets can be launched, the

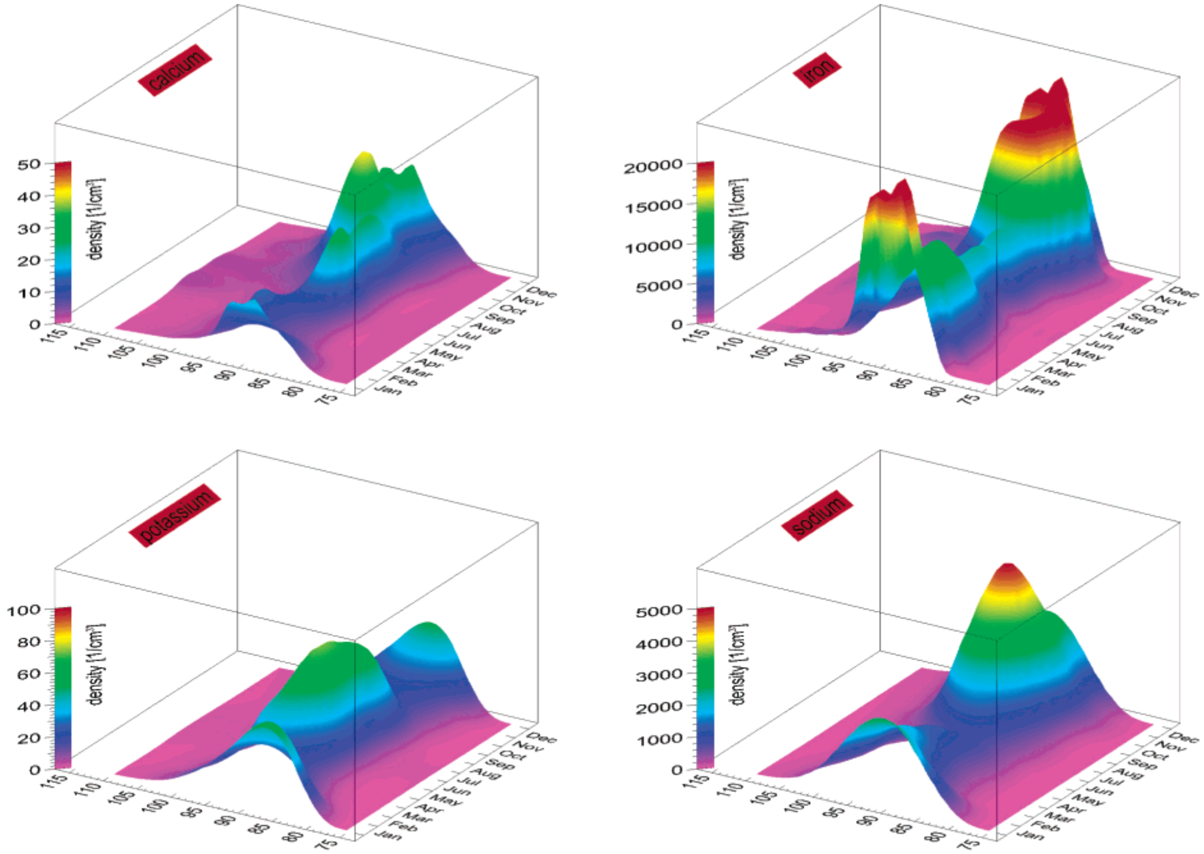

Figure 6. Three-dimensional mesh plots of the annual variations of the Ca, Fe, K, and Na layers, measured by lidar at mid-latitude sites in the United States and Europe (see the caption to Figure 7 for details). (Reproduced with permission from Gerding, M., et al. *J. Geophys. Res.* **2000**, *105*, 27131.)

motors are relatively expensive for routine measurements, and payload recovery is often difficult.

Nevertheless, there have been a number of measurements of the concentrations of positive metallic ions made by rocket-borne mass spectrometry.[33,34] These flights have been motivated by the link between meteor showers and the abundance of metallic ions and the role of metallic ions in forming sporadic *E* layers (section 6.4) and noctilucent clouds (section 6.5). Metallic ions such as Mg^+ and Fe^+ have also been observed by resonant scattering of sunlight, using spectrometers on space vehicles.[34,49,50]

3.2. Observations of Metallic Species

Figure 6 illustrates the Na, Fe, K, and Ca layers as a function of height and month, observed by lidar at several mid-latitude locations where observations have been made over at least one annual cycle.[51] Figure 7 shows the average annual profiles of these four metal layers. Historically, the Na layer has been studied in far greater detail than the other metal layers.[3] The column density of Na is about 5×10^9 atoms cm^{-2}, although this can vary by a factor of 10 depending on time and location. The layer exhibits a seasonal variation with a wintertime maximum. The variation is latitude-dependent: at low latitudes the winter enhancement is only a factor of about 1.3,[52] whereas at mid-latitudes the wintertime enhancement is approximately a factor of 3[46] and more than 10 in the polar regions.[53,54] This appears to reflect the sensitivity of the Na abundance to temperature, because the seasonal variation in temperature increases toward the poles (Figure 1b). The height of the peak of the Na layer varies between 88 and 92 km, with the highest peak heights occurring during summer.[53-55] The full width at half-maximum (fwhm) of the layer is about 10 km, and it is usually characterized by strikingly small scale heights of 2−3 km on the top side of the layer and less than 2 km on the bottom side[56] (the scale height is the distance over which the concentration changes by a factor of *e*). There is a significant increase (30−100%) in the Na column density during the day, which appears to be caused by a combination of photochemistry and the semidiurnal atmospheric tide.[57,58]

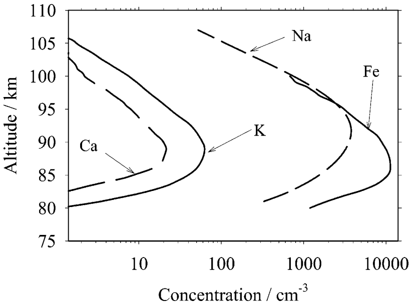

Figure 7. Vertical profiles of the annual mean concentrations at mid-latitudes of Fe (Helmer, M., et al. *J. Geophys. Res.* **1998**, *103*, 10913), Na (Plane, J. M. C., et al. *J. Geophys. Res.* **1999**, *104*, 3773), K (Eska, V., et al. *J. Geophys. Res.* **1999**, *104*, 17173), and Ca (Gerding, M., et al. *J. Geophys. Res.* **2000**, *105*, 27131).

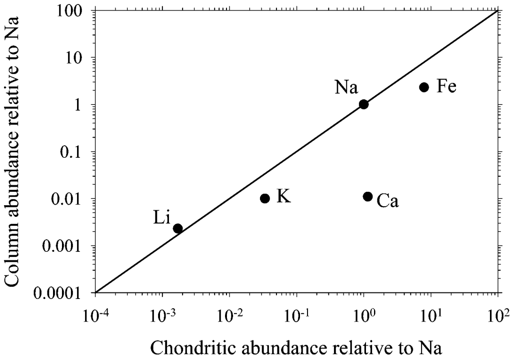

Figure 8. Comparison of the summertime column abundances of Li, K, Fe, and Ca atoms relative to that of Na in the mid-latitude MLT, plotted against their relative elemental abundances in ordinary chondritic meteorites. The data are derived from a variety of sources (see text).

Figure 8 compares the summertime atmospheric column abundances of the Li, K, Fe, and Ca layers to their relative abundances in chondritic meteorites recovered from the Earth's surface. Note that the data set on Li, from the Observatoire d'Haute Provence (France),[59] is much more limited than for the other metals. The alkali metals correlate reasonably well, although the wintertime enhancement of the Li layer is somewhat larger than that of Na,[59] and there is no significant seasonal change in the column abundance of K.[44] Nevertheless, these differences are minor compared to the enormous relative depletion of Ca by a factor of 120−360 depending on season[51] and the significant depletion of Fe by a factor of about 8.[60−63] Another surprising observation is that whereas the mid-latitude Fe and Na layers exhibit a similar early winter maximum and midsummer minimum in concentration, the K and Ca layers have a semiannual variation with a pronounced second maximum in mid-summer,[44,51,64] as shown in Figure 6. Interestingly, very recent measurements at low latitudes (18°N) reveal a smaller seasonal variation in the Fe layer (analogous to the low-latitude Na layer[52]) and a peak density in the early summer.[65] A meridional profile of the K layer has been obtained between 71°S and 45°N using a shipboard K lidar.[64] This shows a 10-fold increase in both the K peak density and column abundance when going from the Antarctic to equatorial regions.

There are other surprising differences in the layers. Compared with the peak of the Na layer, the Li peak is about 4 km higher,[59] while the K peak is on average 1.2 km lower.[51] The Ca peak height at mid-latitudes appears to move from about 92 km in winter to 88 km in summer,[51] which is the reverse of the Na layer. At mid-latitudes, the Fe peak is about 4 km below that of Na, and the Fe layer also has an extremely small bottom scale-height (<1 km) compared with the Na layer (Figure 7). The peak height of Fe is about 87 km in summer and winter and about 2 km higher in spring and autumn.[66] At high latitudes, the Fe peak height seems to be somewhat lower and the layer slightly wider.[67]

In the case of calcium, both Ca and Ca^+ can be monitored simultaneously by lidar, and this has permitted the relationship between the metal atoms and ions to be studied in some detail.[51,68] The annual average Ca^+/Ca column density ratio is about 2.4, whereas the limited set of rocket-borne mass spectrometric data indicates that the ratios of Na^+/Na and Fe^+/Fe are only 0.1 and 0.2, respectively.[34]

Lidar observations have also revealed the phenomenon of sporadic (or sudden) neutral metal layers, which have been observed in the case of Na,[69−71] K,[64] Fe,[72] and Ca.[68] These are very thin, concentrated layers of metal atoms that occur at altitudes between 90 and 110 km, sometimes appearing explosively within a matter of minutes and then surviving for perhaps a few hours. The average width of these sporadic layers is only about 2 km, and their peak concentration can be as much as 40 times the peak of the background metal layer.[73] They have also been observed with a horizontal extent of more than 1000 km.[74] Sporadic layers will be discussed at greater length in section 6.3.

4. Laboratory Studies

The only metal species that can be observed directly in the mesosphere are the atomic neutrals and ions. Knowledge of the chemistry that controls the metal layers and the nature of the metal-containing reservoir species has had to come from a combination of laboratory studies and modeling. Up until the 1980s, laboratory measurements of the rate coefficients for reactions involving metallic species were only available for ion−molecule reactions, which were studied in ion drift tubes.[75] Since then, however, the two classical techniques of flash photolysis and the fast flow tube have been applied with great success to the challenging task of studying reactions of neutral metallic species in the gas phase, at the low temperatures characteristic of the upper atmosphere.[4,5] In addition, a guided-ion beam method[76] has been developed to measure the absolute reaction cross-sections of charge-transfer reactions involving metals, and the techniques of photoelectron spectroscopy[77] and molecular beams[78] have been used to study the production of excited states in metal atom-ozone reactions.

Although most laboratory work has concentrated on sodium chemistry, there is now a growing database on the pertinent reactions of iron, magnesium, calcium, and potassium species. A review of these experimental techniques and the development of theoretical formalisms for interpreting experimental data has been published recently by the author, together with a compilation of recommended rate coefficients.[5] Hence, only a brief discussion will be given in the following sections.

4.1. Experimental Techniques

The flash photolysis technique has been employed in a number of configurations.[3−5] A short pulse of ultraviolet light from a flash lamp or laser is used to photolyze a metal-containing precursor in the gas-phase inside a reaction chamber. The resulting metal atom or metallic fragment is produced in an excess of a molecular reactant diluted in a bath gas (e.g., N_2 or He), and the subsequent reaction is observed by a time-resolved optical monitoring technique such as laser-induced fluorescence, resonance absorption,

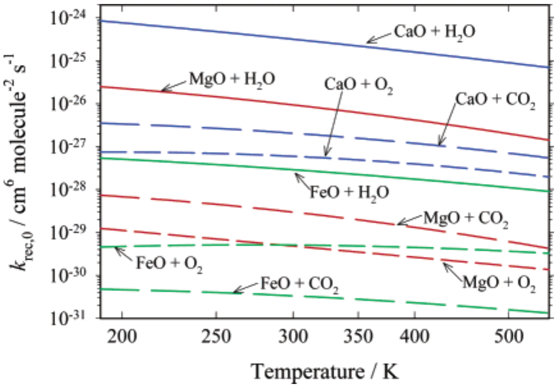

Figure 9. Plots of the low-pressure limiting rate coefficients for the recombination of CaO (blue lines), MgO (red lines), and FeO (green lines) with H_2O, CO_2, and O_2, as a function of temperature. The lines are calculated from RRKM theory that has been fitted to experimental data over a range of temperature and pressure. For further details, see: Rollason, R. J.; Plane, J. M. C. *Phys. Chem. Chem. Phys.* **2001**, *3*, 4733.

or chemiluminescence spectroscopy. Subambient temperatures appropriate to the upper atmosphere are obtained by placing the reactor in a cryogenic chamber.[5]

The pulsed laser photolysis/time-resolved laser induced fluorescence (PLP/LIF) technique has been used in the author's laboratory during the last 5 years to study the reactions of FeO, CaO, and MgO with molecules such as O_3, O_2, CO_2, and H_2O.[79-81] The photolysis laser is an excimer laser operating at either 193 or 248 nm, which is loosely focused in order to achieve multiphoton dissociation of the photolytic precursors to form metal atoms. Organometallic molecules, such as Ca acetyl acetonate ($Ca(C_5H_{10}O_2)_2$) and ferrocene ($Fe(C_5H_5)_2$), are suitable precursors because they are relatively volatile and have strong absorptions in the UV. An oxidant such as O_3 or NO_2 is added to produce the metal oxide. Following the photolysis pulse, the resulting metal oxide species is probed by a pulsed dye laser and the time-resolved LIF signal is recorded. Figure 9 illustrates the rate coefficients for the recombination of the three metal oxides with O_2, CO_2, and H_2O, as a function of temperature (the lines in the figure are semiempirical fits through the experimental data for each reaction—see section 4.2). The formation of the dihydroxide (e.g., $Ca(OH)_2$) is the most exothermic reaction of each metal oxide and also has the largest rate constant, as shown in Figure 9. However, in the MLT the concentration of O_2 is much larger than H_2O or CO_2 (Figure 3a), and so formation of the metal trioxides (e.g., CaO_3) is most rapid in each case. The ion−molecule reactions of Fe^+ with O_3, O_2, and N_2 have also been studied by using the sequential absorption of four photons at 248 nm to produce Fe^+ from ferrocene.[82]

For certain reactions, time-resolved chemiluminescence can be used to monitor the kinetics. For example, the reactions of Ca and Fe with O_3 are so exothermic that the metal oxides are produced in excited electronic states, giving rise to chemiluminescence which can be recorded by photon counting.[83,84] The NaO radical, which does not appear to have a spectroscopic transition suitable for monitoring by LIF, can be detected by producing the radical in a small excess of atomic O and observing chemiluminescence from the reaction $NaO + O \rightarrow Na(^2P_J) + O_2$.[85]

The PLP/LIF technique has also been employed recently[86] to measure the absolute photolysis cross-sections of the sodium-containing molecules NaO, NaO_2, NaO_3, NaOH, and $NaHCO_3$, using a Raman-shifted excimer laser as the pulsed photolysis source and detecting the Na photofragment by LIF. By operating the excimer either with ArF (193 nm) or KrF (248 nm) and using H_2 or D_2 in the Raman cell, cross-sections were measured at a large number of individual wavelengths between 190 and 400 nm.[86]

The fast flow tube technique is particularly useful for studying the reactions of metallic compounds with radicals such as O and H.[87-89] The time resolution required for kinetic measurements is obtained by setting up a rapid flow of a carrier gas (e.g., N_2, He, or Ar) down a tube to an observation point, where at least one of the reactants or products is monitored. In most flow tube arrangements, one reactant is added to the carrier gas flow at the upstream end of the tube and the second is added further downstream through a moveable injector. The rate of reaction is then measured by changing the distance between the injection and observation points and hence altering the reaction time. When studying the kinetics of metallic species, it is important to take account of the strong radial concentration gradient that develops, because these species are deposited with close to unit efficiency on the flow tube walls.[89] Conventionally, subambient reaction temperatures are obtained by enclosing the flow tube in a jacket circulating a cryogenic liquid.[90] An alternative method is to use a supersonic expansion of the flow through a Laval nozzle, which can provide temperatures down to a few Kelvin.[91]

In the last 5 years, flow tubes have been used to study three aspects of mesospheric metal chemistry. The first was an investigation of Na ion−molecule chemistry to explain the formation of sporadic Na layers in the lower thermosphere. This involved a low-temperature (90−250 K) study of the kinetics of cluster formation between Na^+ and N_2, O_2 or CO_2, as well as the reactivity of the resulting cluster ions with atomic O.[90] The mechanism that was constructed from the results of the laboratory study appears to provide a convincing explanation for sporadic Na layer formation (section 6.3).

A second aspect of metal chemistry that has been studied recently using a flow tube is the Chapman mechanism for the production of $Na(^2P_J)$ and hence the Na nightglow at 589 nm in the upper atmosphere.[92] In this challenging experiment, the branching ratio for $Na(^2P_J)$ production from the reaction between $NaO(A^2\Sigma^+)$ and O was determined. The importance of this work is discussed in section 6.1.

Flow tubes have also been used to study the reactions of metal reservoir species, such as NaOH and $NaHCO_3$ in the case of sodium[88] and FeO_2, FeO_3, $Fe(OH)_2$, and FeOH in the case of iron,[89] with atmospheric species such as O, H, and O_3. Figure 10

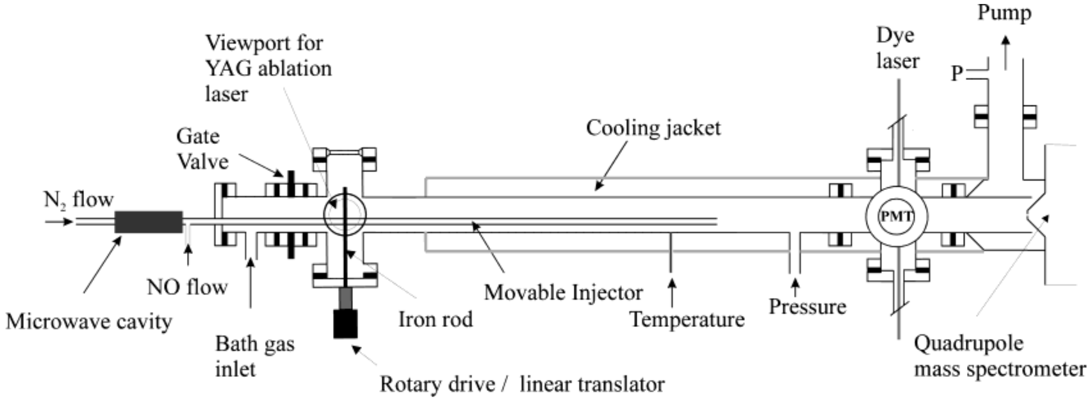

Figure 10. Fast flow tube for studying the reactions of Fe-containing species with atmospheric constituents. (Reproduced with permission from Self, D. E.; Plane, J. M. C. *Phys. Chem. Chem. Phys.* **2003**, *5*, 1407.)

is a schematic diagram of the fast flow tube used to study the reactions of both neutral and ionic Fe-containing species.[89] The stainless steel tube extends from the laser ablation cell at the upstream end through the reaction zone to the spectroscopic cell. Downstream of the cell is a quadrupole mass spectrometer which samples along the cylindrical axis of the tube through an orifice in the center of a skimmer cone. The flow of carrier gas (N_2 for neutrals, He for ions) enters the tube upstream of the ablation cell and exits through a throttle valve to a booster/rotary pump combination providing a large volume displacement rate.

The source of Fe-containing species is the pulsed ablation of a pure iron rod, using a loosely focused Nd:YAG laser ($\lambda = 532$ nm, pulse energy = 22−100 mJ). The rod is rotated and translated to ensure that a fresh surface of iron is presented to each successive laser shot to keep the resulting pulses of ablated Fe as uniform as possible. The pulses of Fe and Fe^+ are then entrained in the carrier gas and transported down the tube at velocities in excess of 10 m s^{-1}. Fe was detected by LIF in the spectroscopic cell using a pulsed dye laser and Fe^+ by the mass spectrometer operating in a time-resolved pulse-counting mode. Neutral Fe-containing reactant species (FeO, FeO_2, etc.) were produced in situ from atomic Fe via the addition of appropriate oxidants (NO_2, O_2) just downstream of the ablation cell. FeO^+ was produced by adding N_2O. Further downstream in the reaction zone, reactants such as O, H, and O_3 were added through a sliding silica injector.

Atomic O was prepared by microwave discharge of N_2, followed by immediate titration with NO (i.e., $NO + N \rightarrow O + N_2$), and the O concentration measured by the standard titration with NO_2.[93] Atomic H was prepared by the microwave discharge of H_2, and the absolute [H] was determined by titration with NO_2 and mass spectrometric detection of the change in NO_2. The pulses of Fe (or Fe^+) were recorded at different flow times in order to measure the loss of the metallic species by radial diffusion to the walls of the tube, as well as the broadening of the pulses through axial diffusion. One major advantage of working with pulses is that the flow velocity of the ions down the tube can be measured directly, whereas when using a continuous flow of ions as in most conventional flow tubes, the plug velocity has to be corrected to account for the efficient wall losses which create strong radial gradients.[88] To determine rate coefficients, a full kinetic model of the flow tube was developed which included diffusion and the wall losses of Fe-containing species and reagents such as atomic O and H.[89] Figure 11 shows the resulting Arrhenius plots for the reactions of FeO, FeO_2, and FeO_3 with atomic O. The atmospheric implications of this study are discussed in section 5.1.

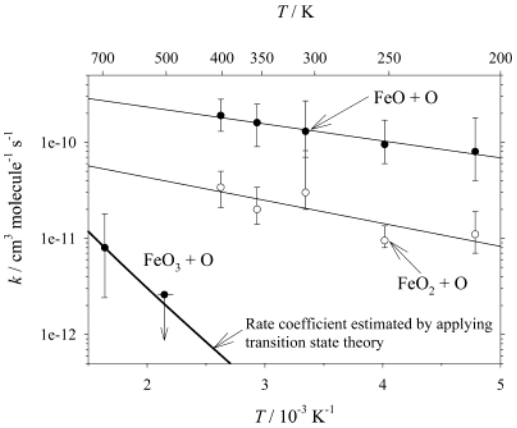

Figure 11. Arrhenius plots for the reactions of FeO, FeO_2, and FeO_3 with atomic O, measured using the apparatus illustrated in Figure 10. (Adapted from Self, D. E.; Plane, J. M. C. *Phys. Chem. Chem. Phys.* **2003**, *5*, 1407.)

4.2. Theoretical Methods

Ab initio quantum calculations, combined with statistical rate methods, such as transition-state theory and Rice−Ramsberger−Kassel−Marcus (RRKM) theory, provide a framework for interpreting experimental measurements and then for extrapolating to the temperature and pressure regimes of the upper mesosphere that are often not experimentally accessible. Quantum calculations on reaction intermediates and transition states also enable reaction pathways and hence mechanisms to be elucidated.

An ab initio quantum calculation provides an approximate solution to the Schrödinger equation within the Born−Oppenheimer approximation. From this solution various molecular properties can be determined, including the optimized geometry, vibrational frequencies, dipole moment, and heat of formation of the molecule. For metal-containing

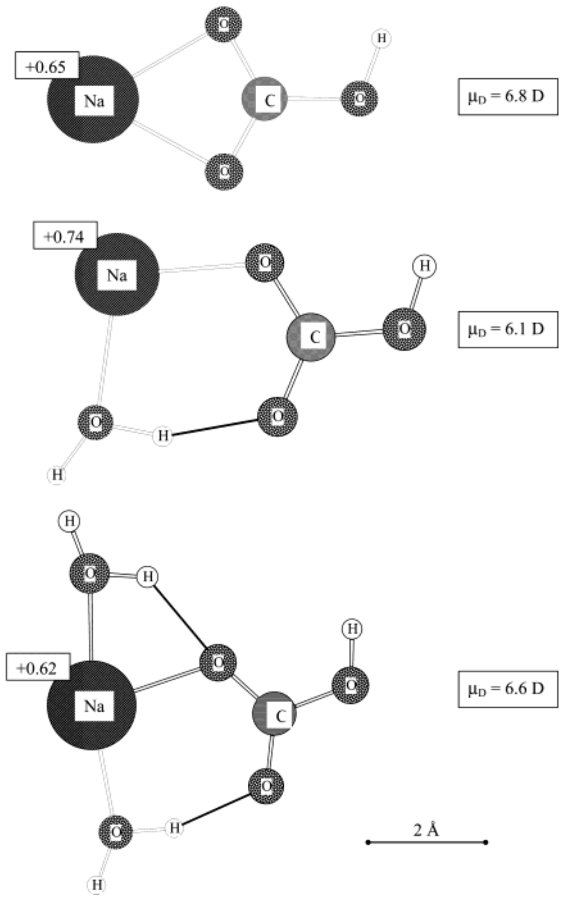

Figure 12. Geometries and dipole moments (μ_D) of $NaHCO_3$ and the first and second H_2O clusters, calculated at the B3LYP/6-311+G(2d,p) level of theory. All structures are planar. The signed number on the Na atom is the Mulliken charge. (Adapted from Plane, J. M. C. *Ann. Geophys.* **2000**, *18*, 807.)

species, such theoretical information is particularly important, because of the difficulty of measuring these quantities in the gas phase. It is worth noting, however, that some data has been obtained from infrared spectroscopy on metallic species deposited into inert gas matrices.[94] Also, high-temperature thermochemical (and kinetic) data have been obtained from flame photometry[95] and the technique of coupling a Knudsen cell to a mass spectrometer.[96]

Reactions involving metallic species often involve electronic potential energy surfaces that change from being covalent to largely ionic in character. When carrying out ab initio calculations, it is therefore important to employ a theoretical method which includes some degree of electron correlation, together with a reasonably large flexible basis set (the basis set describes the atomic orbitals in the molecule). The author has found that the hybrid density functional/Hartree–Fock B3LYP method together with the large 6-311+G(2d,p) basis set, which includes both polarization and diffuse functions, produces good agreement with the experimental data that exist on various Na-, Ca-, and Fe-containing species.[79–81,88] Highly accurate calculations using coupled cluster methods and very large basis sets have been applied recently to neutral and ionized Na and K molecules.[97–99]

As an example of the use of ab initio calculations to address an atmospheric problem, a recent study[100] was carried out to test the hypothesis that a molecule like $NaHCO_3$ could bind sufficiently strongly to H_2O to provide a nucleating agent for noctilucent cloud formation (section 6.4). Figure 12 illustrates the optimized geometries and dipole moments of $NaHCO_3$ and the first and second H_2O clusters. Several conclusions can be drawn. First, the dipole moment of $NaHCO_3$ (6.8 D) is very large. Hence, the rate constant of the clustering reaction with H_2O will be governed by a strong dipole–dipole interaction and as a consequence be very fast. Second, the two H_2O molecules are bound directly to the Na atom, which has an effective (Mulliken) charge of +0.65, and the binding is further stabilized by hydrogen bonds with the bicarbonate anion (shown as thin black lines in Figure 12). Hence, the binding energies of the first and second H_2O molecules are substantial: 70 and 55 kJ mol^{-1}, respectively. Third, even after the addition of two H_2O molecules, the cluster has a large dipole moment, which will facilitate its further growth. Indeed, modeling shows that at H_2O mixing ratios of a few parts per million (typical of the MLT—Figure 3a), runaway nucleation of H_2O around $NaHCO_3$ to form an ice particle should occur at temperatures below 150 K.[100]

The results of ab initio calculations can also be used in statistical rate theories to predict rate coefficients. This is particularly useful when combined with experimental data: the theory is constrained by experiment within the experimental temperature and pressure range and is then used to extrapolate with some confidence outside it. A recent example of this process involved theoretical modeling of the reactions that occur over the $FeO + O \rightarrow FeO_2 \rightarrow Fe + O_2$ potential surface[89]

$$FeO + O \rightarrow Fe + O_2 \tag{8}$$

$$Fe + O_2\ (+M) \rightarrow FeO_2 \text{ or } OFeO \tag{$-$8a}$$

$$Fe + O_2 \rightarrow FeO + O \tag{$-$8b}$$

The forward and reverse bimolecular reactions have been studied at low and high temperatures, respectively, and the recombination of Fe and O_2 to form FeO_2 has been measured over an intermediate temperature range.[89] This presents the opportunity to see if there is a consistent kinetic model that can account for the experimental measurements on reactions 8, −8a, and −8b, over a large range of temperature (200–2000 K). Figure 13a illustrates the stationary points on the lowest-lying potential energy surface for reaction 1, which has quintet spin multiplicity. There are two minima, corresponding to the $FeO_2(^5A_1)$ superoxide that forms initially when Fe and O_2 recombine and the more stable $OFeO(^5B_1)$ dioxide, which forms initially when O adds to FeO. These isomeric forms are connected through a saddle point. Figure 13a shows that this saddle point is well below the asymptotic energies of both $Fe + O_2$ and $FeO + O$ and should therefore not play a significant role in either reaction 8 or −8b.

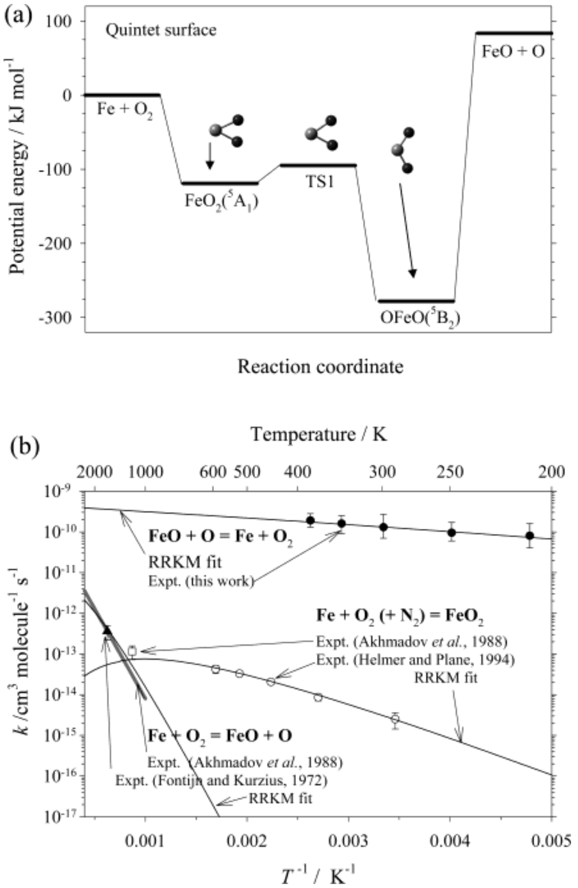

Figure 13. (a) Lowest energy (quintet) potential energy curve for the Fe + O_2 ↔ FeO + O system, calculated at the B3LYP/6-311+G(2d,p) level of theory. (b) RRKM calculated rate coefficients (thin solid lines) at a pressure of 20 Torr over the temperature range of 200−2000 K, compared with experimental measurements (referenced in parentheses). (Reproduced with permission from Self, D. E.; Plane, J. M. C. *Phys. Chem. Chem. Phys.* **2003**, *5*, 1407.)

RRKM theory was then applied to this system. An RRKM calculation solves the master equation describing the time evolution of the populations of the rovibrational states of the newly formed adduct. The microcanonical rate coefficients governing the dissociation of each rovibrational state of the adduct back to the reactants can be computed efficiently by using inverse Laplace transformation[101] to link them directly to the high-pressure limiting recombination coefficient, $k_{rec,\infty}$. For the recombination reactions of many metallic species, $k_{rec,\infty}$ is governed by long-range dipole−induced dipole interactions and hence can be calculated analytically. As shown in Figure 13b, the experimental measurements on reactions 8, −8a, and −8b can be modeled very satisfactorily with RRKM theory.[89]

5. Atmospheric Modeling of the Metal Atom Layers

5.1. Modeling the Global Layers

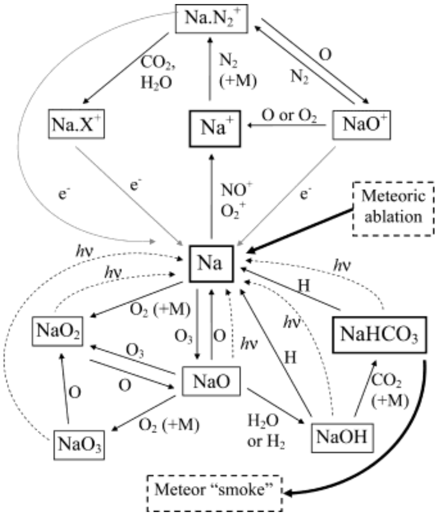

Figure 14. Schematic drawing of the significant gas-phase chemical cycles of sodium in the MLT region. Arrows with solid and broken thin black lines indicate gas-phase and photochemical reactions, respectively, where the rate coefficients have been measured; gray lines indicate reactions that have not been studied experimentally but are included for chemical closure in the model, with estimated rate coefficients. The major sodium species are surrounded by thick-edged boxes. The thick black lines indicate input of Na from meteoric ablation and removal by condensation of $NaHCO_3$ onto metal silicate smoke particles.

Figure 14 is a schematic diagram of the gas-phase chemistry of sodium that is employed in current models.[46,102] Almost all of these reactions have now been studied in isolation under conditions appropriate to the upper mesosphere. Above the atomic Na layer around 90 km, ion chemistry predominates. Na atoms are ionized mostly by charge transfer with the ambient NO^+ and O_2^+ ions, with a small contribution from solar photoionization. Na^+ is then neutralized by forming clusters which undergo dissociative electron recombination. Below 90 km, Na becomes converted to the stable reservoir $NaHCO_3$, via a series of steps beginning with the oxidation of Na by O_3 to NaO. As shown in Figure 14, species such as NaO, NaOH, and $NaHCO_3$ are converted back to Na by reaction with O and H. Hence, the nighttime Na layer only exists at a height above which O and H are also abundant at night. For this reason, the small scale height on the underside of the Na layer correlates closely with the shelf of atomic O (Figure 3b).[55] The chemistry of potassium[64] is probably similar, although this impression is based on a limited number of laboratory studies.[5]

The chemistries of iron, magnesium, and calcium are somewhat different from that of sodium.[51,89,102−104] Figure 15 is a schematic diagram of the gas-phase chemistry of iron, which is based on recent work by the group at the University of East Anglia.[79,82,83,89,105−107] Unlike Na^+ which is chemically inert, the Fe^+ ion has a half-filled outer s orbital and reacts with O_3 and O_2 to form FeO^+ and FeO_2^+, respectively.[82] The rate of neutralization of these metal ions is governed by a competition between O and electrons for the metal oxide ions (section 6.3).

The removal of metal atoms on the underside of the layer involves oxidation by O_3 to form neutral metal oxides, followed by recombination with O_2, CO_2, or H_2O to form the trioxide, carbonate, or dihydroxide, respectively. Although $Fe(OH)_2$ is thermodynamically the most stable form of iron,[79] it is formed slowly

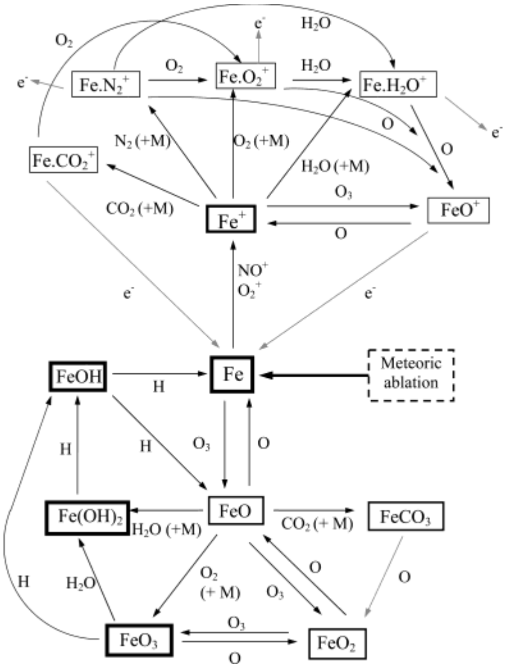

Figure 15. Schematic drawing of the significant chemical cycles of iron in the MLT region. Arrows with solid thin black lines indicate gas-phase reactions with measured rate coefficients; gray lines indicate reactions that have not been studied experimentally but are included for chemical closure in the model, with estimated rate coefficients. The major iron species are surrounded by thick-edged boxes.

because of the extreme dryness of the upper mesosphere and it also reacts relatively rapidly with atomic H.[89] It therefore appears that FeOH is the major iron reservoir below the peak of the Fe layer.[107] The small scale height of less than 2 km on the underside of the Fe layer is then explained by the rapid chemical turnover time of FeOH (3−5 h), compared with a vertical transport time of 10−50 h (depending on season). It is possible that FeOH is oxidized by O_3 to form FeOOH.[107] This oxy−hydroxide is the stable building block of the mineral goethite, which has been detected in stratospheric particles of meteoric origin.[108]

A major review of the modeling of metal layers in the MLT has been published recently.[6] The most common type of model that has been employed is a 1-dimensional model where the metal chemistry is assumed to be in steady state at each height level in the model.[29,46,51,64,104,109,110] Such a model makes the following assumptions: meteoric ablation is the major source of a metal in the mesosphere; gas-phase chemistry is fast on the time-scale of vertical transport; and the metal chemistry is closed. That is, all the constituent species cycle between each other (as shown in Figures 14 and 15), so that no species provides a permanent sink in the upper mesosphere.

Taking iron as an example, the continuity equation for the *i*th Fe-containing species with concentration n_i is given by

$$\frac{\mathrm{d}n_i}{\mathrm{d}t} - P_i + L_i \_\, I_\mathrm{i} + \nabla\Phi_i = 0 \qquad \text{(III)}$$

where P_i and L_i are the chemical production and loss

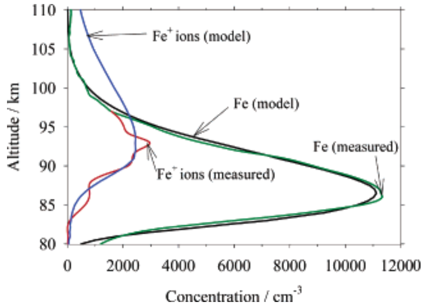

Figure 16. Comparison of the mean annual Fe layer observed by lidar at 40°N (courtesy of C. S. Gardner, University of Illinois at Urbana) and an average Fe^+ profile at mid- and high latitudes (courtesy of E. Kopp, University of Bern), with simulations from the UEA 1-D mesospheric model using the chemistry in Figure 15.

terms, respectively, I_i is the injection rate from meteoric ablation, and Φ_i is the vertical flux of *i*. Summing over all iron-containing species *i* and applying the law of mass action to P_i and L_i, we obtain

$$\frac{\mathrm{d}n(\mathrm{Fe})}{\mathrm{d}t} = \sum_i (I_i - \nabla\Phi_i) = I(\mathrm{Fe}) - \nabla\Phi(\mathrm{Fe}) \qquad \text{(IV)}$$

where *n*(Fe) is the total iron concentration, *I*(Fe) is the total injection rate, and Φ(Fe) is the total flux of all iron species. Under time-averaged conditions, both sides of eq IV should be zero. A further assumption is that the rate of partitioning of a metal among its constituent species is rapid on the time scale of vertical mixing. Hence, a chemical steady state operates at each altitude. Since the transport of all the iron constituents is governed by the same eddy diffusion coefficient up to the turbopause at about 105 km, the vertical flux of total iron at height *z* is then given by

$$\Phi(\mathrm{Fe}) = -K_{zz}\left[\frac{\partial n(\mathrm{Fe})}{\partial z} + n(\mathrm{Fe})\cdot\left(\frac{1}{H} + \frac{1}{T}\frac{\partial T}{\partial z}\right)\right] \qquad \text{(V)}$$

where K_{zz} is the vertical eddy diffusion coefficient, *H* is the atmospheric scale height, and *T* is the temperature. Note that Φ(Fe) is equal to the integrated ablation rate of iron from *z* upward, under time-averaged conditions. Hence, eq V can be solved to obtain the vertical profile of *n*(Fe). The concentrations of the constituent Fe species at each altitude *z* are then computed by assuming a chemical steady state governed by the reactions illustrated in Figure 15. Application of the steady state requires the concentration profiles of the neutral minor species O_3, O, H, H_2, H_2O, and CO_2 and the charged species NO^+, O_2^+, and e^-, which govern the iron chemistry. These can be obtained off-line from measurements or other models.

Figure 16 compares the annual-average model predictions of the Fe and Fe^+ profiles at mid-latitudes with lidar observations of the Fe layer at 40°N[66,104] and an average of rocket-borne mass spectrometric measurements of Fe^+ at mid- and high latitudes.[33] As Figure 16 shows, very satisfactory agreement can be obtained.[107] The total ablation flux of Fe is the single adjustable parameter in the model. Interestingly, the fitted value for the flux is 3.1×10^3 atom cm^{-2} s^{-1}, which is only about 3% of the meteoric iron entering the atmosphere if the total interplanetary dust particle flux is about 50 t d^{-1} (section 2). This may lend support to the smaller total flux measurements of around 12 t d^{-1} reported by the large aperture radar at Arecibo.[21] However, it should be noted that the ablation flux is balanced by downward transport through eddy diffusion (eqs IV and V), and there is some uncertainty in the magnitude of K_{zz}.[46]

Models using the sodium chemistry in Figure 14 are able to reproduce very satisfactorily the observed *nighttime* Na layer as a function of season and latitude.[29,46] However, a recent laboratory study[86] of the photochemistry of sodium species has shown that the major reservoir, $NaHCO_3$, has a sufficiently large photolysis cross-section below 240 nm that its photolysis lifetime is only a few hours in the MLT. This implies that there should be a large increase in Na below 90 km during the day as $NaHCO_3$ is photolyzed—however, this is not observed.[57,58] The most likely reason is the permanent removal of $NaHCO_3$ onto meteoric smoke below 80 km, as shown in Figure 14. This topic is discussed further in section 6.5.

Models for Fe, K, and Ca have also been published recently.[51,64,102,104,110] As Figure 7 shows, there are differences in the heights and shapes of these layers with respect to the Na layer. These differences are largely explained by the differences in chemistry described above. However, differences in chemistry are not able to explain the enormous deviations in the metal abundances from their expected chondritic ratios (Figure 8). The most plausible explanation for these deviations is differential meteoric ablation,[32,51,64] discussed in section 2.

There are cases where the assumptions of the steady-state approach are not valid, and a fully time-dependent model is required.[6] These include modeling the transport of metal ions into the thermosphere, where metal ions act essentially as tracers of transport phenomena,[109−111] and modeling the impact of meteor showers where injection time-scales can be fast relative to chemistry.[112] A further example is considered in the next section.

5.2. Gravity Wave Interactions with the Metal Layers

Observing the spectra of gravity waves that reach the MLT and being able to parametrize the effects of gravity wave breaking is crucial for understanding and modeling the general circulation of the atmosphere (section1). There are two major techniques for observing gravity waves in the MLT. An airglow layer (section 6.1) can be observed using an all-sky camera, which employs a charge-coupled device (CCD) detector behind an appropriate lens and interference filter.[113] This produces an image of the airglow intensity across the sky. The variations in airglow intensity result from waves displacing parcels of air vertically. This causes a heating (cooling) because of adiabatic compression (rarefaction) as the parcel moves down (up), and the reactions producing the airglow emission are often quite T-dependent. Furthermore, as shown in Figure 3b, many of the species such as O, H, and O_3 that are involved in airglow emissions have mixing ratios that change significantly with height, so that a vertical displacement produces a change in the local concentration.[114] Airglow observations are best suited to studying waves with a vertical wavelength $\lambda_z > 12$ km (i.e., greater than the width of the airglow layer) and a horizontal wavelength $\lambda_x < 300$ km (i.e., within the field of view of the camera).

The other major technique for studying waves is the metal resonance lidar, which can observe a wave propagating through one of the meteoric metal layers. In the case of the Na wind/temperature lidar, measuring the horizontal wind field and temperature perturbations provides important additional information for wave analysis.[42] In contrast to airglow measurements, gravity wave observations by lidar require that $\lambda_z < 20$ km, since the metallic layers extend vertically over about this distance, and that λ_x is as long as possible, because the lidar is observing in a Eulerian framework.[42]

One question that arises is whether the metals are suitable inert tracers of atmospheric motion or whether the apparent dynamical perturbation is amplified by a fast chemical response to changes in temperature or the concentrations of minor species. From the opposite point of view, can the response of a metal layer to gravity-wave perturbations be used to test a model of the metal chemistry, in essence using the atmosphere as a large-scale chemical reactor?

In fact, several studies have shown that the Na layer is effectively a conservative tracer of short-period gravity waves.[87,102,115] However, the case of Fe is more interesting.[107] To illustrate this, consider the simple case of a single monochromatic gravity wave in the presence of zero mean winds. Under these conditions, the perturbed atmospheric density, ρ, relative to the unperturbed density, ρ_u, is given by[107,114]

$$\frac{\rho}{\rho_u} = e^{((\xi/H\gamma)(\gamma - 1))} \tag{VI}$$

where H is the scale height and γ is the ratio of specific heats (section 1.4). The parameter ξ is defined by

$$\xi = \gamma H.\ln\left[1 + \frac{\epsilon}{\gamma - 1}e^{\beta(z - z_0)}\cos(\omega t - kx + m(z - z_0))\right] \tag{VII}$$

where ϵ is the wave amplitude at altitude z_0, $1/\beta$ is the amplitude growth length (= $2H$ for an undamped waves), ω is the intrinsic frequency, $m = 2\pi/\lambda_z$ is the vertical wavenumber; and $k = 2\pi/\lambda_x$ is the horizontal wavenumber. The perturbed concentration of a minor component, with unperturbed concentration n_u and scale height H_n is then given by

$$\frac{n(z)}{n_u(z)} = e^{\xi((1/H_n) - (1/\gamma H))} \tag{VIII}$$

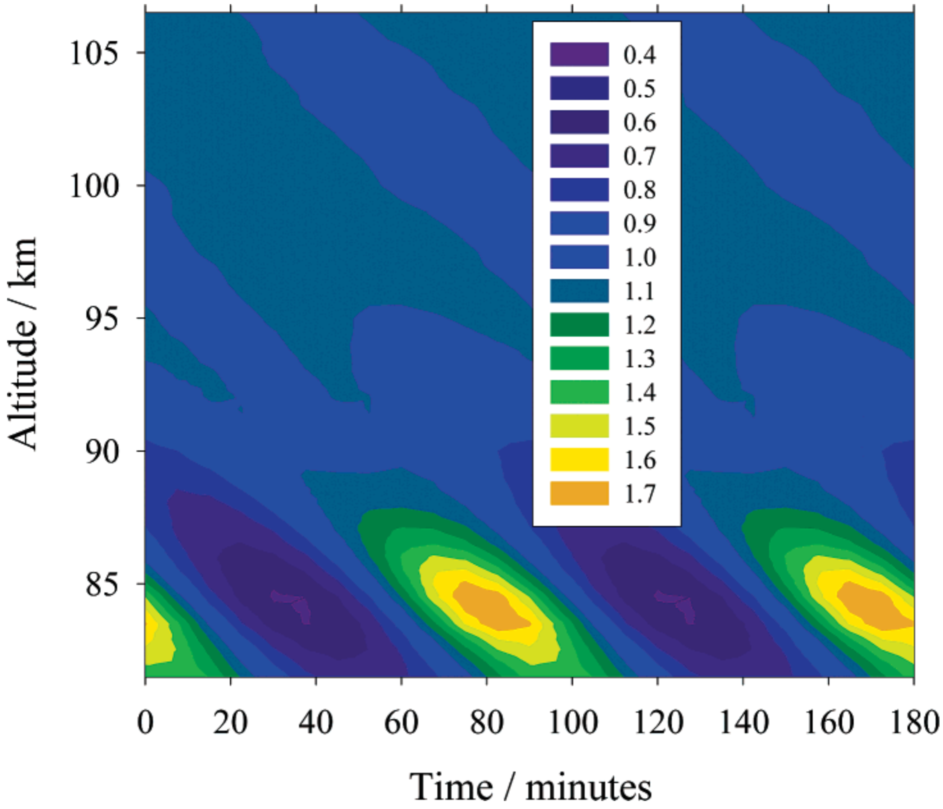

Figure 17. Chemical amplification factor (defined in section 5.2) for the Fe layer during the passage of an atmospheric gravity wave with a period of 90 min and a vertical wavelength of 15 km. The conditions are June at 40°N.

Finally, the perturbed temperature is related to the unperturbed temperature, T_u, by

$$\frac{T(z)}{T_u(z)} = \frac{\rho_u(z)}{\rho(z)} \tag{IX}$$

Perturbations caused by the propagation of gravity waves can now be introduced into the Fe model by using eqs VI−IX to describe the time-dependent variations in temperature, total atmospheric density, and the concentrations of the minor species that drive the iron chemistry (i.e., H, O, O_3, H_2, H_2O, CO_2, NO^+, O_2^+, and e^-). As an example, the model was run for a gravity wave with the following parameters: $\epsilon = 0.05$ at $z_0 = 90$ km, saturated ($\beta = 0$ km^{-1}), $\lambda_z = 15$ km, and period τ ($= 2\pi/\omega$) of 90 min. To analyze the role of chemistry in amplifying (or quenching) the dynamical perturbations to the Fe layer, the model was rerun with the metal atoms acting as conserved tracers, i.e., the time-averaged profile of Fe was calculated and then perturbed by the wave with the chemistry switched off, so that there was no exchange between atomic Fe and the major reservoir species (FeOH and Fe^+). Figure 17 is a contour plot of the chemical amplification factor for Fe versus altitude and time, where the amplification factor is defined as the ratio of Fe calculated with full chemistry to that of Fe as a conserved tracer. This model run is for June (at 40°N), when the amplification factor was found to be largest.

Above 90 km there is relatively little amplification (±10%), whereas the chemical amplification factor becomes much larger below 87 km. For instance, on the underside of the layer at 84 km, the factor ranges from 0.4 to 1.7 at different phases of the wave. This pronounced chemical amplification is caused mainly by two roughly equal factors. First, the underside of the Fe layer is highly sensitive to O, H, and O_3. These species are all strongly coupled and exhibit significant wave-driven perturbations because of the steep falloff in O between 85 and 80 km (Figure 3b). Second, the Fe chemistry is quite temperature-dependent, both because of the activation energies of reactions such as the reaction between FeO_3 and O (Figure 11) and also because of the *T*-dependence of the odd-oxygen and hydrogen chemistry (reactions 1−5). These modeling predictions demonstrate the potential for using wave-driven perturbations to test chemical models in the MLT.

6. Atmospheric Phenomena Involving Meteoric Metals

6.1. Sodium D-Line Airglow

The airglow is a faint, continuous glow in the atmosphere between 40 and 400 km that is observed at all latitudes. It consists of atomic and molecular emission lines, bands, and continua, mostly from electronic spectral transitions. It is caused by chemiluminescent reactions, driven directly or indirectly by the large concentrations of atomic O that persist during both night and day above 80 km (Figure 3b), and in the daytime by solar radiation stimulating fluorescence or producing electronically excited photofragments. Chapman[116] postulated the following sequence of reactions to account for the Na *D*-line emission from $Na(^2P_J)$ in the nightglow

$$Na + O_3 \rightarrow NaO + O_3 \qquad (9)$$

$$NaO + O \rightarrow Na(^2P_J, {}^2S) + O_2 \qquad (10)$$

Historically, there have been two problems associated with validating the Chapman mechanism. The first was that reactions 9 and 10 have to be fast enough to generate the observed *D*-line emission intensity of 50−200 R (1 Rayleigh = 10^6 photons cm^{-2} s^{-1}). In fact, laboratory measurements have now confirmed that both reactions *are* extremely fast.[5,117] Reaction 9, which is rate determining because $[O_3] \ll [O]$ (Figure 3b), proceeds via the electron jump (or harpoon) mechanism.[117] The second problem was the size of the branching ratio, *f*, for production of $Na(^2P_J)$ in reaction 10. An estimate of *f* has been derived from of a field experiment in Brazil, where a rocket carrying a sodium photometer to measure the *D*-line emission profile was launched through the Na layer while a ground-based lidar simultaneously observed the Na atom concentration.[48] Analysis of the data using a geophysical model of the Na layer showed that *f* lay in the range 0.05−0.2, with a best estimate of 0.1.[48] Even though a more recent combined rocket and lidar experiment in Puerto Rico produced a lower estimate for *f* of around 0.03,[118] these estimates are considerably larger than an early laboratory measurement which reported that *f* was less than 0.01.[119]

This apparent disagreement has now been resolved through a series of elegant laboratory experiments. First, it was shown that reaction 9 produces NaO almost entirely in the low-lying $NaO(A^2\Sigma^+)$ excited electronic state rather than the $^2\Pi$ ground state.[77,78] The NaO(A) state has a long radiative lifetime and is not quenched efficiently, so that in the mesosphere reaction 10 involves mostly NaO(A) rather than NaO(X). Second, a recent flow-tube experiment showed that *f* for NaO(A) + O is 0.14 ± 0.04.[92] This measurement thus reconciled the field observations with the underlying chemical physics and showed that the earlier laboratory estimate[119] of *f* was so small because it involved the reaction between ground-state NaO(X) + O.

The ratio between the intensity of the D_2 line at 589.0 nm and that of the D_1 line at 589.6 nm should be 2.0, if $Na(^2P_{3/2})$ and $Na(^2P_{1/2})$ are produced according to their statistical spin−orbit weights. A ratio of 2.0 in the nightglow spectrum was in fact reported, nearly 25 years ago.[120] However, recent analysis of high-resolution airglow spectra taken with the Keck telescope in Hawaii shows that the ratio actually varies between about 1.3 and 1.9 (T. Slanger, SRI, Menlo Park, personal communication). The ratio appears to have a seasonal dependence with higher values during winter, when temperatures in the MLT are higher (Figure 1). The author and A. Saiz-Lopez (University of East Anglia) have since confirmed, using an airborne spectrometer flying between 40° and 50°N during November 2002, that the *D*-line ratio is indeed highly variable. The ratio was found to oscillate between 1.4 and 2.0 (average 1.8), changing over horizontal distances of 50−100 km. This completely unexpected finding is difficult to explain within the current understanding of the Chapman mechanism.

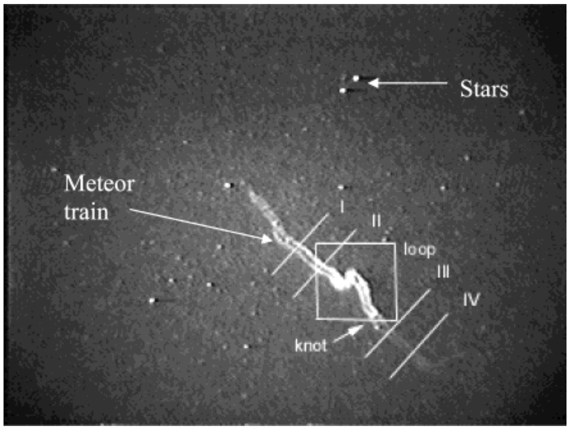

Figure 18. Intensified video image of a persistent Leonid meteor train seen 45 s after the fireball created by a meteoroid with a mass of about 0.1 km. The altitudes marked on the image are as follows: 86 (I), 89 (II), 95 (III), and 97 (IV) km. The distance between points I and IV of the train is about 23 km. (Adapted from Jenniskens, P., et al. *Earth Moon Planets* **2000**, *82*, 471.)

6.2. Persistent Meteor Trains

The bright fireballs of fast meteors sometimes leave a long-lasting glow that is called a *persistent train*. Figure 18 illustrates an example of a Leonid meteor train, 45 s after the fireball. Although the trains are often visible for many minutes, the luminous mechanism itself is poorly understood. The first optical spectra of long-lasting persistent trains were obtained in 1907 by simple visual inspection, which indicated that there are two bright lines in the green and yellow, tentatively identified as $Mg(4^3S - 3^3P_J)$ at 517.3 and 518.4 nm and $Na(3^2P_J - 3^1S)$ at 589.0 and 589.6 nm.[121] Slitless spectrographs have been used subsequently[122] to observe persistent trains, although their wavelength resolution is poor. Most recently, telescopes linked by fiber optic to spectrographs with CCD cameras have been employed.[123]

It is generally believed that the luminosity of persistent trains is fueled by reactions involving O_3 and atomic O, efficiently catalyzed by metals from the freshly ablated meteoroid.[124,125] Probably the most intense single emission arises from the Na *D*-line, almost certainly through the Chapman airglow mechanism (reactions 9 and 10).[124,126] However, recent observations of a persistent train using both a Na lidar and a narrow-band CCD camera showed that Na *D* emission contributed only a fraction of the total luminosity.[127] Molecular emission bands also arise from

$$Fe + O_3 \rightarrow FeO(^5\Delta \text{ etc.}) + O_2 \qquad (11)$$

$$FeO + O \rightarrow Fe + O_2 \qquad (12)$$

where reaction 11 is sufficiently exothermic to produce FeO in excited electronic states, leading to emission in the orange arc bands between 570 and

630 nm with about a 2% efficiency.[83] These FeO bands have been observed recently in a persistent train spectrum.[123] Other metals such as Ca and K will also contribute to the overall emission intensity, but the ablated concentrations of these metals are much lower (Figure 7). Emission also arises from $O(^1S)$, OH, and excited states of O_2 such as the $b^1\Sigma_g^+$ state, produced by the elevated O atom concentrations in the train.[126−128]

Figure 18 reveals a very curious feature of many persistent trains: the appearance of twin trails along sections of the train that exhibit very little turbulent mixing (the sections outside the box in Figure 18), compared with the billowy sections of the train where eddy diffusion operates as expected (the knot and loop inside the box in Figure 18). It had been commonly assumed that the twin trails are due to the meteor train forming a luminous cylindrical tube with bright walls and a dark center which, when viewed from below, appeared as two thin trails.[128,129] The proposed explanation for the dark center is that O_3, which fuels the chemiluminescent reactions discussed above, has been consumed by thermal dissociation in the initially very hot train and by fast metal-catalyzed removal (e.g., reactions 9 + 10 and reactions 11 + 12). Photolysis of O_3 by UV emission from the meteor fireball may also be important. However, recent attempts to explain the twin trails using the luminous tube model have shown that it is not possible to achieve a high enough contrast between the tube walls and the center when viewed from below, and the evolution of the trail widths and their separation is also difficult to simulate.[127,128] Furthermore, temperature measurements using a Na lidar have shown that the walls of the apparent tube are 20−50 K hotter than the tube center or surrounding atmosphere; this cannot be explained by chemical or frictional heating.[126] In summary, our understanding of persistent trains is far from satisfactory.

6.3. Sporadic Layers

Sporadic *E* layers are thin layers of metallic ions, typically only 1−3 km wide, that occur between 90 and 140 km.[130] They have a significant impact on radio communications, both by facilitating over-the-horizon high-frequency communication and by obscuring space-to-ground communications, depending on the time of day and transmission frequency. Sporadic *E* layers are often associated with meteor showers, which provide a large input of metallic ions,[33] and also with auroral activity where electron precipitation causes enhanced ionization of the MLT region.[35,111,131] The metallic ions are concentrated into layers at the null points of wind shears, because the ions experience $V \times B$ forces when undergoing horizontal wind transport across the Earth's magnetic field lines.[130] Metal atoms generally have low ionization potentials (<8 eV), and so metal ions are formed readily by charge transfer or photoionization

$$\mathrm{Fe} + \mathrm{O_2}^+ \text{ (or NO}^+\text{)} \rightarrow \mathrm{Fe}^+ + \mathrm{O_2} \text{ (or NO)} \quad (13)$$

$$\mathrm{Fe} + h\nu \rightarrow \mathrm{Fe}^+ + e^- \quad (14)$$

Metallic ions have lifetimes of at least several days in the thermosphere above 100 km and can be transported to heights of over 400 km.[49,110,111,132] Their long lifetimes are a result of their being monatomic, so that dielectric recombination (e.g., $\mathrm{Fe}^+ + e^- \rightarrow \mathrm{Fe} + h\nu$) is very slow, with a rate coefficient of $\approx 4 \times 10^{-12}$ cm^3 molecule^{-1} s^{-1}. Furthermore, even though metallic ions can be quite reactive (reaction 15), atomic O quickly reduces metallic molecular ions back to atomic ions (reaction 16), competing effectively with dissociative electron recombination (reaction 17) above 100 km[107]

$$\mathrm{Fe}^+ + \mathrm{O_3} \rightarrow \mathrm{FeO}^+ + \mathrm{O_2} \quad (15)$$

$$\mathrm{FeO}^+ + \mathrm{O} \rightarrow \mathrm{Fe}^+ + \mathrm{O_2} \quad (16)$$

$$\mathrm{FeO}^+ + e^- \rightarrow \mathrm{Fe} + \mathrm{O} \quad (17)$$

In explaining the intriguing phenomenon of sporadic neutral metal layers, it has been noted that sporadic layers commonly occur together with sporadic *E* layers.[133−135] Sporadic neutral layers can be produced from metallic ions by first forming molecular ions or ion clusters, which then undergo dissociative electron recombination. The process of ion cluster formation is extremely sensitive to altitude. For example, the ion−molecule reaction scheme in Figure 14 has been used to explain how a sporadic Na layer can form from a layer of Na^+ ions.[136] Na^+ recombines with N_2 to form the weakly bound $Na\cdot N_2^+$ cluster ion. However, above 100 km, this ion will generally be broken down by atomic O to reform Na^+. Below 100 km, switching reactions with CO_2 (or less frequently with H_2O, which is less abundant—Figure 3a) cause stable clusters to form that are immune to attack by O and will eventually undergo dissociative electron recombination to produce Na. If a sporadic *E* layer forms and then descends, the release of Na can turn on very rapidly because the formation rate of $Na\cdot N_2^+$ depends on $[N_2]^2$ and the ratio of $[CO_2]/[O]$ increases markedly below 100 km (Figure 3).[136]

Figure 19 compares an observation of a sporadic Na layer with a model prediction using this ion−molecule chemistry.[137] The model predicts a sudden release of Na when the sporadic *E* layer reaches 96 km (Figure 19a), in excellent agreement with the lidar observations (Figure 19b). Although this mechanism appears to provide a convincing explanation for sporadic neutral layers below 100 km (where ion−molecule reactions become fast),[137−139] there may well be other mechanisms, such as auroral precipitation acting on meteoric smoke particles[71,73,140,141] or metal-containing molecules.[142] Wind shears and local temperature enhancements may also play a role.[69,143,144] Finally, recent observations[145] at both the North and South Poles of large sporadic Fe layers at heights around 106 km, where ion−molecule chemistry should be ineffective, indicate that the subject of sporadic layer formation is far from being well understood.

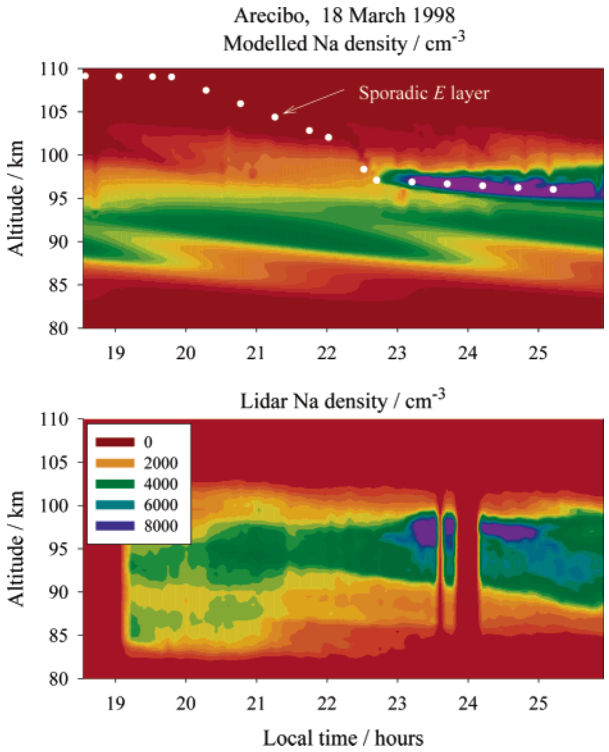

Figure 19. Example of a sporadic Na layer forming at 96 km over the Arecibo Observatory, Puerto Rico, at about 2315 h and persisting for 2 h. (Top) A model prediction using the ion−molecule chemistry in Figure 14; the white dots show the height of a sporadic *E* layer measured simultaneously using the Arecibo incoherent scatter radar. (Bottom) Observations of the Na density using a resonance lidar. See Collins, S., et al. *J. Atmos. Solar-Terr. Phys.* **2002**, *64*, 845 for further details.

6.4. Noctilucent Clouds and Climate Change

Noctilucent clouds (NLCs) are thin clouds (1−2 km thick) that occur during the summer at high latitudes, at an altitude of about 83 km (that is, at least 60 km higher than any other cloud types in the atmosphere).[146] As shown in Figure 1, this is when the mesopause temperature falls below about 150 K.[147] NLCs can be observed visually from the ground when the sun is more than 10° below the horizon (so that the lower atmosphere is in darkness). The forward scattering of sunlight by the clouds in the upper mesosphere then gives rise to spectacularly beautiful displays around local midnight. In the daytime NLCs can be monitored by lidar,[148,149] by satellite[150−152] when they are termed polar mesospheric clouds (PMCs), and by radar[153−155] when they are termed polar mesospheric summer echoes (PMSEs).

NLCs were first reported during June 1885 over middle and northern Europe.[156] Since then it appeared that the clouds were being observed more frequently,[157] leading to speculation that they are an early warning of climate change in the MLT.[158] NLCs are composed of ice particles,[150] and since they occur in an extremely dry region of the atmosphere (Figure 3a), this would indicate either that the MLT is getting colder or that the H_2O concentration is rising, so that the H_2O frost point is reached more frequently. H_2O is produced from the oxidation of CH_4 in the lower mesosphere, and CH_4 levels have certainly risen as a result of intensive agriculture and natural gas usage, so that the concentration of H_2O in the MLT has probably increased by about 50% since 1850.[158]

Nevertheless, it seems that cold temperatures at the summer mesopause are the most important factor in producing NLC.[147,158] A dramatic cooling of the middle mesosphere (50−75 km), at a rate of about 0.5 year^{-1}, has in fact been recorded over the past 40 years. The longest record is a set of rocket-borne temperature measurements going back to the 1960s, which shows a consistent decrease over a range of latitudes.[159] This is confirmed by Rayleigh lidar measurements over more than 20 years at a midlatitude site (Observatoire d′Haute Provence).[160]

In fact, a cooling of the mesosphere is expected because of anthropogenic emissions of infrared-active gases such as CO_2 and methane. Unlike the lower atmosphere, an increase of these gases at heights above 30 km causes radiative cooling. Interestingly, models of greenhouse gas cooling underestimate the observed rate of cooling by about an order of magnitude,[161] indicating that there may also be a long-term change occurring in the meridional circulation (Figure 2). It is worth emphasising that the mesosphere is probably the most sensitive region of the atmosphere to climate change.[162] This is because the change in temperature over the last two decades (≈ -10 K) is similar to the diurnal temperature variation (unlike the troposphere, stratosphere, or thermosphere) and should therefore be easier to detect.

A temperature decrease in the middle mesosphere should cause contraction in a vertical direction and, to maintain hydrostatic balance, layered phenomena higher up in the atmosphere should move downward. There is indeed some evidence for this: the height of a radio reflection layer around 82 km has decreased by about 30 m year^{-1},[163] and satellite drag at a constant geometric height in the thermosphere has also decreased by about 10% since the 1970s.[164]

In contrast, there is no evidence that the height at which NLCs appear has changed significantly in the 120 years since they were observed. This is probably now explained by a recent report that there have been no long-term changes in the summer mesospheric temperature profile *at high latitudes*.[165] Further analysis of the NLC occurrence statistics (M. Gadsden, personal communication) has also shown that there has probably not been the marked secular increase that was reported earlier.[157]

Recent developments in lidar, radar, and satellite technology have enabled NLCs to be observed by remote sensing with much greater sophistication.[149] The clouds tend to form when the mesopause temperature drops below about 150 K, producing particle densities ranging from about 200−2000 cm^{-3}. The nuclei on which H_2O condenses to form NLC could be *D* region proton hydrates,[166−168] metallic molecules with large dipole moments[100] (section 4.2), or meteoric smoke particles[23] (section 6.5). Nucleation presumably occurs at the mesopause (87 km). As the particles grow they settle gravitationally, eventually sublimating in the warmer mesosphere at about 82 km. It is believed that PMSEs are caused mainly by

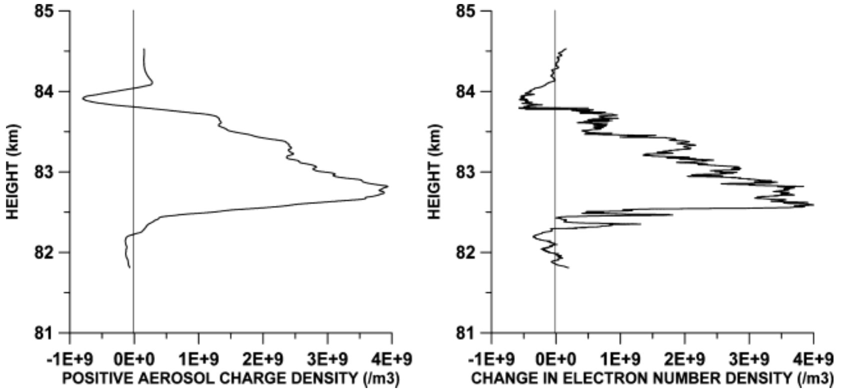

Figure 20. Measurements of positively charged aerosol and electron density by electrostatic probes mounted on the front and rear of a rocket payload over Andoya, Norway (69°N) during June 1994 [courtesy of T. Blix, Norwegian Defense Research Establishment]. The measurements are described in Havnes, O., et al. *J. Geophys. Res.* **1996**, *101*, 10839.

small particles with a radius less than 10 nm, which are negatively charged by the attachment of electrons. The radar is then scattered from the sharp gradient in the free electron density around the cloud.[155,169] Multicolor lidar observations tend to sample larger particles with a median radius around 30 nm.[149] The largest particles, which are visible as NLCs, have radii in excess of 50 nm.[158]

In the past few years, rocket-borne instruments have revealed some surprises. For instance, charged particle collectors have shown that that NLC particles are sometimes *positively* charged, with an enhanced cloud of electrons around them, as shown in Figure 20.[170,171] The only likely explanation for this observation is that very efficient photoelectric emission from the particles is occurring at $\lambda > 180$ nm. This indicates that the ice surface of the particles has become coated with metallic species,[172] lowering the photoelectric work function. This process needs to be verified in the laboratory.

Rocket experiments have also shown that atomic O is significantly depleted in the vicinity of a cloud. This was presumed to occur through the surface-catalyzed recombination of O.[173] However, the uptake coefficient of O on ice has recently been measured over the temperature range 100−150 K; under mesospheric conditions, the ice-catalyzed removal of O is too slow by about an order of magnitude.[174] Instead, it appears that O (and O_3) is removed by gas-phase catalytic cycles driven by odd hydrogen species (reactions 1−5).[174] There are likely to be two sources of additional odd hydrogen. First is the Lyman-α photolysis of enhanced gas-phase H_2O around the clouds; indeed, an enhancement of H_2O by a factor of 3 was recently reported from observations by a limb-scanning satellite.[151] Second is the Lyman-α photolysis of the ice particles themselves.[174]

Substantial depletions of metal atoms have also been observed in the meteoric metal layers when an NLC is present: both the Na layer[175] and K layer[176] are characterized by a very steep scale height on the underside of the metal layer. Given that the upper mesosphere is continuously sunlit in the polar summer and that the gas-phase sinks such as sodium bicarbonate photolyze quite readily,[86] it is difficult to see how such a small scale height can be maintained without an additional sink for the metal in the aerosol layer. Very recently, X. Chu and C. S. Gardner (University of Illinois, personal communication) reported depletions of more than an order of magnitude within the Fe layer over the South Pole when an NLC is simultaneously observed.

Finally, an analysis of a 15-year series of lidar measurements of the sodium layer at 23°S appeared to show that the centroid height of the layer was decreasing in altitude at about 50 m $year^{-1}$.[177] This was consistent with the rates of cooling in the middle mesosphere referred to above. However, a new analysis including more recent Na layer observations at the same site shows that there has been essentially no change to the layer over the longer period 1972−2001 (B. R. Clemesha, INPE, Sao Paulo, personal communication). It is therefore becoming apparent that the dramatic rate of cooling in the middle mesosphere is a mid-latitudes phenomenon.

6.5. Meteor Smoke in the Middle and Lower Atmosphere

In the middle mesosphere it is presumed that the metallic compounds polymerize together with silicon oxides (also produced by meteoric ablation) to form metal-rich particles, known as meteoric smoke.[23,24] Polymerization probably occurs rapidly because several of these species, particularly the metal monohydroxides, carbonates, and bicarbonates, have large dipole moments (section 4.2). In order for these particles to remain suspended above 80 km for more than a few hours against gravitational settling, they have to be smaller than 2 nm in radius.[23,24] Over a period of several days, these tiny particles are likely to grow as a result of condensation and coagulation and sediment into the lower mesosphere.[24] It has been speculated that the observed increase in the H_2O mixing ratio around 70 km at low latitudes could be explained by the reaction between atomic O and H_2, catalyzed on the surface of these meteoric smoke particles.[178]

In the stratosphere it has been proposed that meteoric metals could have a significant impact on the chlorine-catalyzed removal of ozone in several ways. First, the metal compounds are chemically alkaline and react rapidly with hydrogen chloride produced by chlorofluorocarbon destruction in the upper stratosphere.[3,5] The resulting metal chlorides will photolyze readily to yield atomic Cl and the metal atom, which will rapidly reform a metallic compound and the sequence will repeat. The overall effect is to catalyze the photolysis of HCl to atomic Cl and increase O_3 depletion.[179] However, the metal chlorides could also polymerize rapidly because of the long-range dipole−dipole forces between them and eventually diffuse out of the stratosphere, thus removing a significant fraction of atmospheric chlorine.[180]

Metal-rich particles also appear to provide condensation nuclei for the sulfate aerosols in the lower stratosphere,[16,181] which are the precursors of polar stratospheric clouds. The seasonal meridional circulation in the mesosphere (Figure 2) should result in a large flux of meteoric smoke descending into the winter polar vortex. Interestingly, the downward flux of essentially alkaline smoke from the mesosphere approximately balances the nitric acid removed when the lower stratosphere becomes denitrified by the formation of polar stratospheric clouds during the polar night.[182] Finally, the transport of this material, which is probably rich in water-soluble iron, may have a significant impact in fertilizing the Fe-deficient Southern Ocean around Antarctica, which is far removed from sources of continental aeolian dust.[183,184]

7. Summary

Meteoric metals clearly undergo an extremely diverse chemistry in the MLT, a fascinating and relatively unexplored region of the atmosphere. Much progress has been achieved in understanding this chemistry through a combination of lidar, satellite, and rocket measurements, laboratory studies, and atmospheric modeling. Nevertheless, many intriguing problems remain to be addressed. A selection of these include the process of differential meteoric ablation (section 2); the surprising differences between the Na and K layers (section 3.2); the very high metal ion/metal atom ratio of Ca, compared to the other metals (section 3.2); gravity-wave-driven perturbations of metal chemistry (section 5.2); the variable Na D_2/D_1 ratio in the nightglow (section 6.1); the chemistry of persistent meteor trains (section 6.2); the appearance of substantial sporadic Fe and Na layers well above 100 km (section 6.3); the observation of positively charged particles in noctilucent clouds (section 6.4); and the formation of meteor smoke and its impact in the lower atmosphere (section 6.5).

8. References

(1) Slipher, V. M. *Publ. Astron. Soc. Pacific* **1929**, *41*, 262.
(2) Bernard, R. *Z. Phys.* **1938**, *110*, 291.
(3) Plane, J. M. C. *Int. Rev. Phys. Chem.* **1991**, *10*, 55.
(4) Plane, J. M. C.; Helmer, M. In *Research in Chemical Kinetics*; Hancock, G., Ed.; Elsevier Science: Amsterdam, 1994; Vol. 2.
(5) Plane, J. M. C. In *Meteors in the Earth's Atmosphere*; Murad, E., Williams, I. P., Eds.; Cambridge University Press: Cambridge, 2002.
(6) McNeil, W. J.; Murad, E.; Plane, J. M. C. In *Meteors in the Earth's Atmosphere*; Murad E., Williams, I. P., Eds.; Cambridge University Press: Cambridge, 2002.
(7) Williams, I. P. In *Meteors in the Earth's Atmosphere*; Murad, E., Williams, I. P., Eds.; Cambridge University Press: Cambridge, 2002.
(8) Ceplecha, Z.; Borovicka, J.; Elford, W. G.; Revelle, D. O.; Hawkes, R. L.; Porubcan, V.; Simek, M. *Space Sci. Rev.* **1998**, *84*, 327.
(9) Jenniskens, P. *Earth Planets Space* **1998**, *50*, 555.
(10) Hughes, D. W. In *Cosmic Dust*; McDonnell, J. A. M., Ed.; Wiley: London, 1978.
(11) Baggaley, W. J. In *Meteors in the earth's atmosphere*; Murad, E., Williams, I. P., Eds.; Cambridge University Press: Cambridge, 2002.
(12) Hughes, D. W. *Endeavour* **1997**, *21*, 31.
(13) Wasson, J. T.; Kyte, F. T. *Geophys. Res. Lett.* **1987**, *14*, 779.
(14) McBride, N.; Green, S. F.; McDonnell, J. A. M. *Adv. Space Res.* **1999**, *23*, 73.
(15) Love, S. G.; Brownlee, D. E. *Science* **1993**, *262*, 550.
(16) Cziczo, D. J.; Thomson, D. S.; Murphy, D. M. *Science* **2001**, *291*, 1772.
(17) Janches, D.; Mathews, J. D.; Meisel, D. D.; Zhou, Q. H. *Icarus* **2000**, *145*, 53.
(18) Mathews, J. D.; Meisel, D. D.; Hunter, K. P.; Getman, V. S.; Zhou, Q. *Icarus* **1997**, *126*, 157.
(19) Pellinen-Wannberg, A.; Wannberg, G. *J. Geophys. Res.* **1994**, *99*, 11379.
(20) Close, S.; Hunt, S.; Minardi, M.; McKeen, F. *Radio Sci.* **2000**, *35*, 1233.
(21) Mathews, J. D.; Janches, D.; Meisel, D. D.; Zhou, Q. H. *Geophys. Res. Lett.* **2001**, *28*, 1929.
(22) Love, S. G.; Brownlee, D. E. *Icarus* **1991**, *89*, 26.
(23) Kalashnikova, O.; Horanyi, M.; Thomas, G. E.; Toon, O. B. *Geophys. Res. Lett.* **2000**, *27*, 3293.
(24) Hunten, D. M.; Turco, R. P.; Toon, O. B. *J. Atmos. Sci.* **1980**, *37*, 1342.
(25) Rietmeijer, F. J. M. *Meteor. Planet. Sci.* **2000**, *35*, 1025.
(26) Rietmeijer, F. J. M. In *Meteors in the earth's atmosphere*; Murad, E., Williams, I. P., Eds.; Cambridge University Press: Cambridge, 2002.
(27) Jones, J.; Kaiser, T. R. *Mon. Not. R. Astr. Soc.* **1966**, *133*, 411.
(28) Fegley, J. B.; Cameron, A. G. W. *Earth Planet. Sci. Lett.* **1987**, *82*, 207.
(29) McNeil, W. J.; Murad, E.; Lai, S. T. *J. Geophys. Res.* **1995**, *100*, 16847.
(30) Mason, B. *Handbook of elemental abundances of the elements in meteorites*; Gordon and Breach: Newark, NJ, 1971.
(31) McNeil, W. J.; Lai, S. T.; Murad, E. *J. Geophys. Res.* **1998**, *103*, 10899.
(32) von Zahn, U.; Gerding, M.; Hoffner, J.; McNeil, W. J.; Murad, E. *Meteor. Planet. Sci.* **1999**, *34*, 1017.
(33) Kopp, E. *J. Geophys. Res.* **1997**, *102*, 9667.
(34) Grebowsky, J. M.; Aikin, A. C. In *Meteors in the earth's atmosphere*; Murad, E., Williams, I. P., Eds.; Cambridge University Press: Cambridge, 2002.
(35) Grebowsky, J. M.; Goldberg, R. A.; Pesnell, W. D. *J. Atmos. Solar-Terr. Phys.* **1998**, *60*, 607.
(36) Kane, T. J.; Gardner, C. S. *Science* **1993**, *259*, 1297.
(37) Chu, X. Z.; Pan, W. L.; Papen, G.; Gardner, C. S.; Swenson, G.; Jenniskens, P. *Geophys. Res. Lett.* **2000**, *27*, 1807.
(38) Gerding, M.; Alpers, M.; Hoffner, J.; von Zahn, U. *J. Geophys. Res.* **1999**, *104*, 24689.
(39) von Zahn, U.; Hoffner, J.; McNeil, W. J. In *Meteors in the earth's atmosphere*; Murad, E., Williams, I. P., Eds.; Cambridge University Press: Cambridge, 2002.
(40) Hunten, D. M. *Space Sci. Rev.* **1967**, *6*, 493.
(41) States, R. J.; Gardner, C. S. *J. Atmos. Sci.* **2000**, *57*, 66.
(42) Gardner, C. S.; Taylor, M. J. *J. Geophys. Res.* **1998**, *103*, 6427.
(43) Manson, A. H.; Meek, C. E.; Qian, J.; Gardner, C. S. *J. Geophys. Res.* **1998**, *103*, 6455.
(44) Eska, V.; Hoffner, J.; von Zahn, U. *J. Geophys. Res.* **1998**, *103*, 29207.
(45) Yu, J. R.; States, R.; Franke, S. J.; Gardner, C. S.; Hagan, M. *Geophys. Res. Lett.* **1997**, *24*, 1207.
(46) Plane, J. M. C.; Gardner, C. S.; Yu, J. R.; She, C. Y.; Garcia, R. R.; Pumphrey, H. C. *J. Geophys. Res.* **1999**, *104*, 3773.
(47) Chu, X. Z.; Pan, W. L.; Papen, G. C.; Gardner, C. S.; Gelbwachs, J. A. *Appl. Opt.* **2002**, *41*, 4400.
(48) Clemesha, B. R.; Simonich, D. M.; Takahashi, H.; Melo, S. M. L.; Plane, J. M. C. *J. Geophys. Res.* **1995**, *100*, 18909.
(49) Gardner, J. A.; Murad, E.; Viereck, R. A.; Knecht, D. J.; Pike, C. P.; Broadfoot, A. L. *Adv. Space Res.* **1998**, *21*, 867.
(50) Gardner, J. A.; Viereck, R. A.; Murad, E.; Knecht, D. J.; Pike, C. P.; Broadfoot, A. L.; Anderson, E. R. *Geophys. Res. Lett.* **1995**, *22*, 2119.
(51) Gerding, M.; Alpers, M.; von Zahn, U.; Rollason, R. J.; Plane, J. M. C. *J. Geophys. Res.* **2000**, *105*, 27131.
(52) Simonich, D. M.; Clemesha, B. R.; Kirchhoff, V. W. J. H. *J. Geophys. Res.* **1979**, *84*, 1543.
(53) Gardner, C. S.; Senft, D. C.; Kwon, K. H. *Nature* **1988**, *332*, 142.
(54) Kurzawa, H.; von Zahn, U. *J. Atmos. Terr. Phys.* **1990**, *52*, 981.

(55) Plane, J. M. C.; Cox, R. M.; Qian, J.; Pfenninger, W. M.; Papen, G. C.; Gardner, C. S.; Espy, P. J. *J. Geophys. Res.* **1998**, *103*, 6381.
(56) Tilgner, C.; von Zahn, U. *J. Geophys. Res.* **1988**, *93*, 8439.
(57) States, R. J.; Gardner, C. S. *J. Atmos. Sci.* **2000**, *57*, 78.
(58) Clemesha, B. R.; Simonich, D. M.; Batista, P. P.; Kirchhoff, V. *J. Geophys. Res.* **1982**, *87*, 181.
(59) Jegou, J.-P.; Chanin, M.-L.; Megie, G.; Blamont, J. E. *Geophys. Res. Lett.* **1980**, *7*, 995.
(60) Granier, C.; Jegou, J. P.; Megie, G. *Geophys. Res. Lett.* **1989**, *16*, 243.
(61) Alpers, M.; Hoffner, J.; von Zahn, U. *Geophys. Res. Lett.* **1990**, *17*, 2345.
(62) Bills, R. E.; Gardner, C. S. *Geophys. Res. Lett.* **1990**, *17*, 143.
(63) Kane, T. J.; Mui, P. H.; Gardner, C. S. *Geophys. Res. Lett.* **1992**, *19*, 405.
(64) Eska, V.; von Zahn, U.; Plane, J. M. C. *J. Geophys. Res.* **1999**, *104*, 17173.
(65) Raizada, S.; Tepley, C. A. *Geophys. Res. Lett.* **2003**, *30*, 1082.
(66) Kane, T. J.; Gardner, C. S. *J. Geophys. Res.* **1993**, *98*, 16875.
(67) Alpers, M.; Blix, T.; Kirkwood, S.; Krankowsky, D.; Lbken, F. J.; Lutz, S.; von Zahn, U. *J. Geophys. Res.* **1993**, *98*, 275.
(68) Gerding, M.; Alpers, M.; Hoffner, J.; von Zahn, U. *Ann. Geophys.* **2001**, *19*, 47.
(69) Gardner, C. S. *Faraday Discuss.* **1995**, 431.
(70) Batista, P. P.; Clemesha, B. R.; Batista, I. S.; Simonich, D. M. *J. Geophys. Res.* **1989**, *94*, 15349.
(71) Clemesha, B. R. *J. Atmos. Terr. Phys.* **1995**, *57*, 725.
(72) Gardner, C. S.; Kane, T. J.; Senft, D. C.; Qian, J.; Papen, G. C. *J. Geophys. Res.* **1993**, *98*, 16865.
(73) Kane, T. J.; Gardner, C. S.; Zhou, Q.; Mathews, J. D.; Tepley, C. A. *J. Atmos. Terr. Phys.* **1993**, *55*, 499.
(74) Kane, T. J.; Hostetler, C. A.; Gardner, C. S. *Geophys. Res. Lett.* **1991**, *18*, 1365.
(75) Ferguson, E. E.; Fehsenfeld, F. C. *J. Geophys. Res.* **1968**, *73*, 6215.
(76) Levandier, D. J.; Dressler, R. A.; Williams, S.; Murad, E. *J. Chem. Soc., Faraday Trans.* **1997**, *93*, 2611.
(77) Wright, T. G.; Ellis, A. M.; Dyke, J. M. *J. Chem. Phys.* **1993**, *98*, 2891.
(78) Shi, X.; Herschbach, D. R.; Worsnop, D. R.; Kolb, C. E. *J. Phys. Chem.* **1993**, *97*, 2113.
(79) Rollason, R. J.; Plane, J. M. C. *Phys. Chem. Chem. Phys.* **2000**, *2*, 2335.
(80) Plane, J. M. C.; Rollason, R. J. *J. Phys. Chem. A* **2001**, *105*, 7047.
(81) Rollason, R. J.; Plane, J. M. C. *Phys. Chem. Chem. Phys.* **2001**, *3*, 4733.
(82) Rollason, R. J.; Plane, J. M. C. *J. Chem. Soc., Faraday Trans.* **1998**, *94*, 3067.
(83) Helmer, M.; Plane, J. M. C. *J. Chem. Soc., Faraday Trans.* **1994**, *90*, 31.
(84) Helmer, M.; Plane, J. M. C.; Allen, M. R. *J. Chem. Soc., Faraday Trans.* **1993**, *89*, 763.
(85) Cox, R. M.; Plane, J. M. C. *Phys. Chem. Chem. Phys.* **1999**, *1*, 4713.
(86) Self, D. E.; Plane, J. M. C. *Phys. Chem. Chem. Phys.* **2002**, *4*, 16.
(87) Helmer, M.; Plane, J. M. C. *J. Geophys. Res.* **1993**, *98*, 23207.
(88) Cox, R. M.; Self, D. E.; Plane, J. M. C. *J. Geophys. Res.* **2001**, *106*, 1733.
(89) Self, D. E.; Plane, J. M. C. *Phys. Chem. Chem. Phys.* **2003**, *5*, 1407.
(90) Cox, R. M.; Plane, J. M. C. *J. Chem. Soc., Faraday Trans.* **1997**, *93*, 2619.
(91) Le Picard, S. D.; Canosa, A.; Travers, D.; Chastaing, D.; Rowe, B. R.; Stoecklin, T. *J. Phys. Chem. A* **1997**, *101*, 9988.
(92) Griffin, J.; Worsnop, D. R.; Brown, R. C.; Kolb, C. E.; Herschbach, D. R. *J. Phys. Chem. A* **2000**, *105*, 1643.
(93) Kaufman, F. *Proc. R. Soc. A* **1958**, *247*, 123.
(94) Chertihin, G. V.; Saffel, W.; Yustein, J. T.; Andrews, L.; Neurock, M.; Ricca, A.; Bauschlicher, J., C. W. *J. Phys. Chem.* **1996**, *100*, 5261.
(95) Jensen, D. E.; Jones, G. A. *J. Chem. Soc., Faraday Trans.* **1973**, *69*, 1448.
(96) Murad, E. *J. Chem. Phys.* **1980**, *73*, 1381.
(97) Lee, E. P. F.; Wright, T. G. *J. Phys. Chem. A* **2002**, *106*, 8903.
(98) Lee, E. P. F.; Wright, T. G. *Chem. Phys. Lett.* **2002**, *363*, 139.
(99) Lee, E. P. F.; Wright, T. G. *Mol. Phys.* **2003**, *101*, 405.
(100) Plane, J. M. C. *Ann. Geophys.* **2000**, *18*, 807.
(101) Pereira, R. D.; Baulch, D. L.; Pilling, M. J.; Robertson, S. H.; Zeng, G. *J. Phys. Chem. A* **1997**, *101*, 9681.
(102) Plane, J. M. C.; Cox, R. M.; Rollason, R. J. *Adv. Space Res.* **1999**, *24*, 1559.
(103) Plane, J. M. C.; Helmer, M. *Faraday Discuss.* **1995**, 411.
(104) Helmer, M.; Plane, J. M. C.; Qian, J.; Gardner, C. S. *J. Geophys. Res.* **1998**, *103*, 10913.
(105) Plane, J. M. C.; Rollason, R. J. *Phys. Chem. Chem. Phys.* **1999**, *1*, 1843.
(106) Helmer, M.; Plane, J. M. C. *J. Chem. Soc., Faraday Trans.* **1994**, *90*, 395.
(107) Plane, J. M. C.; Self, D. E.; Vondrak, T.; Woodcock, K. R. I. *Adv. Space Res.* **2003**, *In press.*
(108) Rietmeijer, F. J. M. *Planet. Space Sci.* **2001**, *49*, 71.
(109) McNeil, W. J.; Lai, S. T.; Murad, E. *J. Geophys. Res.* **1996**, *101*, 5251.
(110) McNeil, W. J.; Lai, S. T.; Murad, E. *Adv. Space Res.* **1998**, *21*, 863.
(111) MacDougall, J. W.; Plane, J. M. C.; Jayachandran, P. T. *J. Atmos. Solar-Terr. Phys.* **2000**, *62*, 1169.
(112) McNeil, W. J.; Dressler, R. A.; Murad, E. *J. Geophys. Res.* **2001**, *106*, 10447.
(113) Tang, J.; Liu, A. Z.; Swenson, G. R. *Geophys. Res. Lett.* **2002**, *29*, art. no.-1966.
(114) Swenson, G. R.; Gardner, C. S. *J. Geophys. Res.* **1998**, *103*, 6271.
(115) Hickey, M. P.; Plane, J. M. C. *Geophys. Res. Lett.* **1995**, *22*, 2861.
(116) Chapman, S. *J. Astrophys.* **1939**, *90*, 309.
(117) Plane, J. M. C.; Nien, C. F.; Allen, M. R.; Helmer, M. *J. Phys. Chem.* **1993**, *97*, 4459.
(118) Hecht, J. H.; Collins, S.; Kruschwitz, C.; Kelley, M. C.; Roble, R. G.; Walterscheid, R. L. *Geophys. Res. Lett.* **2000**, *27*, 453.
(119) Plane, J. M. C.; Husain, D. *J. Chem. Soc., Faraday Trans.* **1986**, *82*, 2047.
(120) Sipler, D. P.; Biondi, M. A. *Planet. Space Sci.* **1978**, *26*, 65.
(121) Trowbridge, C. C. *Ap. J.* **1907**, *26*, 95.
(122) Borovicka, J.; Zimnikoval, P.; Skvarka, J.; Rajchl, J.; Spurny, P. *Astron. Astrophys.* **1996**, *306*, 995.
(123) Jenniskens, P.; Lacey, M.; Allan, B. J.; Self, D. E.; Plane, J. M. C. *Earth Moon Planets* **2000**, *82*, 429.
(124) Kolb, C. E.; Elgin, J. B. *Nature* **1976**, *263*, 488.
(125) Hapgood, M. A. *Nature* **1980**, *286*, 582.
(126) Chu, X. Z.; Liu, A. Z.; Papen, G.; Gardner, C. S.; Kelley, M.; Drummond, J.; Fugate, R. *Geophys. Res. Lett.* **2000**, *27*, 1815.
(127) Kruschwitz, C. A.; Kelley, M. C.; Gardner, C. S.; Swenson, G.; Liu, A. Z.; Chu, X.; Drummond, J. D.; Grime, B. W.; Armstrong, W. T.; Plane, J. M. C.; Jenniskens, P. *J. Geophys. Res.* **2001**, *106*, 21525.
(128) Jenniskens, P.; Nugent, D.; Plane, J. M. C. *Earth Moon Planets* **2000**, *82*, 471.
(129) Kelley, M. C.; Gardner, C.; Drummond, J.; Armstrong, T.; Liu, A.; Chu, X.; Papen, G.; Kruschwitz, C.; Loughmiller, P.; Grime, B.; Engelman, J. *Geophys. Res. Lett.* **2000**, *27*, 1811.
(130) Mathews, J. D. *J. Atmos. Solar-Terr. Phys.* **1998**, *60*, 413.
(131) MacDougall, J. W.; Jayachandran, P. T.; Plane, J. M. C. *J. Atmos. Solar-Terr. Phys.* **2000**, *62*, 1155.
(132) Grebowsky, J. M.; Reese, N. *J. Geophys. Res.* **1989**, *94*, 5427.
(133) Beatty, T. J.; Collins, R. L.; Gardner, C. S.; Hostetler, C. A.; Sechrist, C. F.; Tepley, C. A. *Geophys. Res. Lett.* **1989**, *16*, 1019.
(134) von Zahn, U.; Hansen, T. L. *J. Atmos. Terr. Phys.* **1988**, *50*, 93.
(135) Alpers, M.; Hoffner, J.; von Zahn, U. *J. Geophys. Res.* **1994**, *99*, 14971.
(136) Cox, R. M.; Plane, J. M. C. *J. Geophys. Res.* **1998**, *103*, 6349.
(137) Collins, S. C.; Plane, J. M. C.; Kelley, M. C.; Wright, T. G.; Soldan, P.; Kane, T. J.; Gerrard, A. J.; Grime, B. W.; Rollason, R. J.; Friedman, J. S.; Gonzalez, S. A.; Zhou, Q. H.; Sulzer, M. P.; Tepley, C. A. *J. Atmos. Solar-Terr. Phys.* **2002**, *64*, 845.
(138) Heinselman, C. J.; Thayer, J. P.; Watkins, B. J. *Geophys. Res. Lett.* **1998**, *25*, 3059.
(139) Gong, S. S.; Yang, G. T.; Wang, J. M.; Liu, B. M.; Cheng, X. W.; Xu, J. Y.; Wan, W. *J. Atmos. Sol.-Terr. Phys.* **2002**, *64*, 1957.
(140) von Zahn, U.; Vondergathen, P.; Hansen, G. *Geophys. Res. Lett.* **1987**, *14*, 76.
(141) Heinselman, C. J. *J. Geophys. Res.-Atmos.* **2000**, *105*, 12181.
(142) Rajasekhar, B.; Plane, J. M. C. *Geophys. Res. Lett.* **1993**, *20*, 21.
(143) Gardner, C. S.; Tao, X.; Papen, G. C. *Geophys. Res. Lett.* **1995**, *22*, 2809.
(144) Zhou, Q. H.; Mathews, J. D. *J. Atmos. Terr. Phys.* **1995**, *57*, 1309.
(145) Gardner, C. S.; Papen, G. C.; Chu, X. Z.; Pan, W. L. *Geophys. Res. Lett.* **2001**, *28*, 1199.
(146) Thomas, G. E. *Rev. Geophys.* **1991**, *29*, 553.
(147) Lbken, F. J. *J. Geophys. Res.* **1999**, *104*, 9135.
(148) Alpers, M.; Gerding, M.; Hoffner, J.; von Zahn, U. *J. Geophys. Res.* **2000**, *105*, 12235.
(149) von Cossart, G.; Fiedler, J.; von Zahn, U. *Geophys. Res. Lett.* **1999**, *26*, 1513.
(150) Hervig, M.; Thompson, R. E.; McHugh, M.; Gordley, L. L.; Russell, J. M.; Summers, M. E. *Geophys. Res. Lett.* **2001**, *28*, 971.
(151) Summers, M. E.; Conway, R. R.; Englert, C. R.; Siskind, D. E.; Stevens, M. H.; Russell, J. M.; Gordley, L. L.; McHugh, M. J. *Geophys. Res. Lett.* **2001**, *28*, 3601.
(152) Gadsden, M. *Adv. Space Res.* **2001**, *27*, 1697.
(153) Lbken, F. J.; Rapp, M.; Blix, T.; Thrane, E. *Geophys. Res. Lett.* **1998**, *25*, 893.
(154) von Zahn, U.; Bremer, J. *Geophys. Res. Lett.* **1999**, *26*, 1521.
(155) Blix, T. A. *Adv. Space Res.* **1999**, *24*, 537.
(156) Schrder, W.; Rendtel, J. *Bull. Am. Meteor. Soc.* **1998**, *79*, 324.
(157) Gadsden, M. *Adv. Space Res.* **1997**, *20*, 22097.

(158) Thomas, G. E. *J. Atmos. Terr. Phys.* **1996**, *58*, 1629.
(159) Golitsyn, G. S.; Seminov, A. I.; Shefov, N. N.; Fishkova, L. M.; Lysenko, E. V.; Perov, S. P. *Geophys. Res. Lett.* **1996**, *23*, 1741.
(160) Keckhut, P.; Hauchecorne, A.; Chanin, M. L. *J. Geophys. Res.* **1995**, *100*, 18887.
(161) Rishbeth, H.; Roble, R. G. *Planet. Space Sci.* **1992**, *40*, 1011.
(162) Olivero, J. J.; Thomas, G. E. *Adv. Space Res.* **2001**, *28*, 931.
(163) Taubenheim, J.; Entzian, G.; Berendorf, K. *Adv. Space Res.* **1997**, *20*, 22059.
(164) Keating, G. M.; Tolson, R. H.; Bradford, M. S. *Geophys. Res. Lett.* **2000**, *27*, 1523.
(165) Lbken, F. J. *Adv. Space Res.* **2001**, *28*, 947.
(166) Kopp, E.; Eberhardt, P.; Herrmann, U.; Bjorn, L. G. *J. Geophys. Res.* **1985**, *90*, 3041.
(167) Gumbel, J.; Witt, G. *Geophys. Res. Lett.* **2002**, *29*, art. no.-1782.
(168) Balsiger, F.; Kopp, E.; Friedrich, M.; Torkar, K. M.; Walchli, U.; Witt, G. *Geophys. Res. Lett.* **1996**, *23*, 93.
(169) Havnes, O.; Melandso, F.; Lahoz, C.; Aslaksen, T. K.; Hartquist, T. *Phys. Scr.* **1992**, *45*, 535.
(170) Havnes, O.; Troim, J.; Blix, T.; Mortensen, W.; Naesheim, L. I.; Thrane, E.; Tonnesen, T. *J. Geophys. Res.* **1996**, *101*, 10839.
(171) Croskey, C. L.; Mitchell, J. D.; Friedrich, M.; Torkar, K. M.; Hoppe, U. P.; Goldberg, R. A. *Geophys. Res. Lett.* **2001**, *28*, 1427.
(172) Rapp, M.; Lbken, F. J. *Earth Planets Space* **1999**, *51*, 799.
(173) Gumbel, J.; Murtagh, D. P.; Espy, P. J.; Witt, G.; Schmidlin, F. J. *J. Geophys. Res.* **1998**, *103*, 23399.
(174) Murray, B. J.; Plane, J. M. C. *Adv. Space Res.* **2003**, *31*, 2075.
(175) Hansen, G.; Serwazi, M.; von Zahn, U. *Geophys. Res. Lett.* **1989**, *16*, 1445.
(176) Lbken, F. J.; Hffner, J.; Fricke-Bergmann, C.; Mllemann, A.; Zecha, M.; Rttger, J. *Memoirs of the British Astrononomical Association: Proceedings of Mesospheric Clouds 2002*, Perth, Scotland, 2002; Vol. 45, p 11.
(177) Clemesha, B. R.; Simonich, D. M.; Batista, P. P. *Geophys. Res. Lett.* **1992**, *19*, 457.
(178) Summers, M. E.; Siskind, D. E. *Geophys. Res. Lett.* **1999**, *26*, 1837.
(179) Murad, E.; Swider, W.; Benson, S. W. *Nature* **1981**, *289*, 273.
(180) Lamb, J. J.; Benson, S. W. *J. Geophys. Res.* **1986**, *91*, 6215.
(181) Murphy, D. M.; Thomson, D. S.; Mahoney, T. M. J. *Science* **1998**, *282*, 1664.
(182) Rodriguez, J. M.; Ko, M. K. W.; Sze, N. D. *Geophys. Res. Lett.* **1986**, *13*, 499.
(183) Watson, A. J.; Bakker, D. C. E.; Ridgwell, A. J.; Boyd, P. W.; Law, C. S. *Nature* **2000**, *407*, 730.
(184) Johnson, K. S. *Glob. Biogeochem. Cycle* **2001**, *15*, 61.

CR0205309